buildings

MDPI

Article

Stability Analysis of Coastal Slopes Based on a Semi-Diurnal Tidal Water Level Variation Model

Jiahua Zhang [1,2,*], Yulong Wang [1,2], Yunjun Wei [1,2] and Cheng Yao [2]

[1] Sanya Institute, Hunan University of Science and Technology, Sanya 572024, China; 24020103022@mail.hnust.edu.cn (Y.W.); 23020103019@mail.hnust.edu.cn (Y.W.)
[2] School of Resources Environment and Safety Engineering, Hunan University of Science and Technology, Xiangtan 411201, China; 25020103101@mail.hnust.edu.cn
* Correspondence: 1010090@hnust.edu.cn

Abstract

To investigate the impacts of tidal level fluctuations on the groundwater dynamics and stability of coastal slopes, a numerical simulation framework was developed using the SEEP/W and SLOPE/W modules in GeoStudio. By combining saturated–unsaturated seepage mechanics with the finite element limit equilibrium method, the semi-diurnal tidal cycle was simulated to derive analytical solutions for the internal water-level distribution within the slope, and to assess the factor of safety as well as the geometry of the potential slip surface. By examining the evolutionary patterns of the phreatic surface and pore-water pressure inside the slope, this work elucidates the failure mechanisms of coastal slopes under tidal forcing. The findings demonstrate that tidal fluctuations induce periodic, hysteretic variations in the slope's phreatic surface, which peaks at the conclusion of the rising tide (t = 0 h) and reaches its trough at the end of the falling tide (t = 6 h). Pore-water pressure alterations are predominantly localized in the near-surface region of the slope. The slope's factor of safety exhibits pronounced oscillations in tandem with tidal levels, attaining a maximum at the end of the rising tide (t = 0 h) and a minimum at the end of the falling tide (t = 6 h), thus identifying the falling tide phase as the critical window for instability. Tidal changes exert a comparatively limited influence on the spatial positioning of the slip surface, underscoring the concealed and abrupt nature of tidal impacts on slope stability. Numerical simulation outcomes align closely with theoretical calculations, with small relative errors, which verifies the consistency and effectiveness of the simulation and theoretical calculations.

Keywords: coastal slope; tidal water level; saturated–unsaturated seepage; phreatic line; pore water pressure

Check for updates

Academic Editor: Mijia Yang

Received: 31 March 2026
Revised: 3 May 2026
Accepted: 4 May 2026
Published: 13 May 2026

Copyright: © 2026 by the authors. Licensee MDPI, Basel, Switzerland. This article is an open access article distributed under the terms and conditions of the Creative Commons Attribution (CC BY) license.

1. Introduction

With the continuous progress of engineering projects related to coastal ports, highways, and waterfront industrial zones, the stability problems of coastal slopes have grown increasingly prominent in recent years. As the most dominant hydrodynamic feature in coastal regions, the periodic ebb and flow of tidal levels constantly alter the external hydraulic boundary conditions of slopes. This change further induces the dynamic redistribution of hydraulic head differences both within and outside the slope, thereby driving the complex spatiotemporal evolution of saturated-unsaturated seepage fields inside the slope mass [1]. Such temporal and spatial variations in seepage fields directly alter the

distribution of pore-water pressures within geotechnical media, which further regulates the effective stress state and shear resistance of slope materials. Consequently, tidal action has gradually emerged as a critical inducing factor for the instability and failure of coastal slopes [2–4].

Currently, a wealth of studies have been carried out by researchers worldwide to elucidate the relationship between groundwater dynamics and slope stability [5–8]. Existing inquiries primarily center on conventional operational scenarios, encompassing static groundwater tables, rapid reservoir drawdown, and rainfall infiltration, with a suite of analytical methodologies including the finite element limit equilibrium technique and the strength reduction approach being well-established. Zhou et al. [9] developed a three-dimensional stability assessment model for riverbank slopes during reservoir water level decline, grounded in rigorous limit equilibrium principles, which addresses the inherent limitation of traditional two-dimensional analyses that overlook spatial effects. Xu et al. [10] explored the influences of reservoir water level oscillations on slope stability, along with the impulse wave phenomena induced by slope failures, and determined that the risk of slope instability is notably elevated during the water drawdown period. Considering the spatial distribution characteristics of soil saturation and matric suction, Wang et al. [11] developed an improved layered summation approach to assess the three-dimensional stability of unsaturated soil slopes after rapid water level decline. Through physical model experiments, Wei et al. [12] further uncovered the dominant mechanism governing the deformation of landslides containing weak interlayers under reservoir water level fluctuation; Cao et al. [13] established a nonlinear seepage mechanical model and performed bifurcation analysis for fluid-solid coupling in fractured rock mass, uncovering the saddle-node bifurcation and nonlinear dynamic features of the coupled seepage system. Meanwhile, in terms of tidal-related research, Shaikh et al. [14] derived analytical solutions for groundwater dynamic fluctuations in complex coastal aquifers by comprehensively incorporating the coupling effects of periodic tidal oscillation and rainfall infiltration, and clarified the response law of groundwater levels under dual-factor interference. Kishore et al. [15,16] focused on the complex stress scenarios of coastal geotechnical engineering and performed stability analysis on coastal retaining walls and wharf slopes subjected to the combined action of earthquakes and tsunamis.

Numerical simulation has long served as an indispensable technical tool for analyzing seepage field evolution and slope stability under dynamic groundwater conditions, acting as a critical bridge connecting theoretical derivation and physical model testing. Meanwhile, relevant simulation methodologies and software applications have been continuously optimized and upgraded. Sun et al. [17] established a dynamic correlation model between water level variation and seepage field/stability responses via numerical simulation, explicitly revealing the evolutionary law of safety factors. Tang et al. [18] demonstrated that the determination method of the phreatic surface exerts a decisive influence on numerical calculation results of water-related slope stability, providing novel insights for refined seepage simulation. Huang et al. [19] realized high-precision simulation of the entire slope failure process using the continuous-discrete coupled method, enriching the methodological system of numerical modeling for slope engineering. Through a systematic review, Boruah et al. [20] summarized the research progress of slope stability and deformation analysis under rainfall and seismic loading, highlighting the central role of numerical simulation in multi-factor coupled slope research; Li et al. [21] implemented multi-factor coupled numerical simulation and sensitivity analysis on hysteretic water inrush induced by the activation of small faults in the coal seam floor under mining disturbance, and determined the dominant controlling factors and their sensitivity order for delayed water inrush; Wu et al. [22] adopted numerical methods to thoroughly investigate the failure characteristics of

rainfall-induced saturated–unsaturated landslides and elaborated the intrinsic mechanism whereby seepage evolution governs slope stability. Wang et al. [23] further concluded via numerical simulation that increasing rainfall intensity and duration tend to shift the sliding failure surface toward the shallow layer of slopes and simultaneously reduce the overall safety factor.

In conclusion, prior investigations have yielded substantial achievements in the domain of groundwater-driven slope stability assessment, with well-developed theories and methodologies extensively applied to conventional contexts including reservoir water level oscillations and rainfall infiltration. Numerical simulation and analytical calculation approaches have also been widely adopted in corresponding engineering studies. Notwithstanding, notable limitations remain in current inquiries regarding coastal slopes under cyclic tidal fluctuations. Most preceding work simplifies tidal loading as a static hydraulic boundary or directly adopts analytical frameworks designed for reservoir water level variation, entirely neglecting the cyclic dynamic characteristics of tidal oscillations and the hysteretic behavior of seepage flow, which precludes accurate depiction of the evolution of internal seepage fields and the dynamic changes in slope stability. To bridge these research gaps, the present work develops a numerical simulation model for coastal slopes utilizing GeoStudio software to replicate the semi-diurnal tidal rise-fall cycle. Integrated with limit equilibrium theory, analytical solutions for the internal water level distribution within slopes are derived to elucidate the instability mechanism of coastal slopes under tidal action. The research outcomes are anticipated to offer a dependable reference for stability evaluation and protective design in practical coastal slope engineering projects.

2. Numerical Simulation Model

The model presented in this study is not a real engineering case, but a standardized benchmark model specifically designed for the mutual verification between analytical and numerical solutions. It is used to demonstrate the validity of the theoretical method and the consistency of calculation results, rather than for practical engineering design. The SEEP and SLOPE modules within GeoStudio(v2024.2.1, GEO-SLOPE International Ltd., Calgary, AB, Canada) software are employed to assess the stability of coastal slopes subjected to tidal level oscillations. Initially, the SEEP module is utilized to examine the distribution pattern of the groundwater table within the slope under dynamic tidal conditions. The computed outcomes from the SEEP module are subsequently imported into the SLOPE module, where the entry and exit boundaries of potential slip surfaces are defined. Ultimately, the temporal variation in the stability of the coastal slope is calculated.

2.1. Saturated–Unsaturated Seepage Theory of the SEEP Module

The SEEP module is mainly used to analyze seepage problems and investigate the variation laws of the seepage face in slopes under water level changes and different slope permeability coefficients. First, the seepage-related parameters of the slope rock and soil mass are input, including volumetric water content and hydraulic conductivity. Then, seepage boundary conditions are applied to the slope model. Finally, the distribution of the phreatic surface and the evolution patterns of pore water pressure under various working conditions are calculated.

The SEEP module postulates that water movement within both saturated and unsaturated soils conforms to Darcy's Law. The fundamental distinction lies in the fact that the hydraulic conductivity of unsaturated soil is not an invariable value, but a parameter that varies adaptively in response to the dynamic shifts in soil moisture content and pore water pressure. Integrating the principle of mass conservation, the governing equation for

saturated–unsaturated seepage in soils is consequently derived for analytical purposes [18], as presented in the formula below:

$$\frac{\partial}{\partial x}(k_x\frac{\partial H_w}{\partial x})+\frac{\partial}{\partial y}(k_y\frac{\partial H_w}{\partial y})+Q=m_w\gamma_w\frac{\partial H_w}{\partial t} \quad (1)$$

In the above equation, H_w denotes the total hydraulic head; k_x stands for the permeability coefficient along the x-direction; k_y represents the permeability coefficient along the y-direction; Q corresponds to the boundary flux condition; m_w signifies the specific water capacity; γ_w is the unit weight of water; and t represents the time variable.

Based on the F-X model, the volumetric water content function can be formulated through a closed-form expression incorporating curve-fitting parameters, as presented below:

$$\theta_w=C(\phi)\frac{\theta_{sat}}{\ln\left[e+(\frac{\phi}{a})^{n}\right]^{m}} \quad (2)$$

In the above expression, θ_w stands for the volumetric water content; a, m, and n are fitting parameters that determine the form of the volumetric water content function; $C(\phi)$ corresponds to the specific water capacity associated with matric suction; θ_{sat} is the saturated volumetric water content; and ϕ represents the matric suction.

Based on the F-X model, the hydraulic conductivity function is obtained by integrating the volumetric water content function with the saturated hydraulic conductivity, as presented in the following equation:

$$K_w(\theta_w)=K_{sat}\int_{\theta_{res}}^{\theta_w}\frac{\theta_w-x}{\phi^2(x)}dx\Big/\int_{\theta_{res}}^{\theta_{sat}}\frac{\theta_{sat}-x}{\phi^2(x)}dx \quad (3)$$

In the foregoing equation, K_w signifies the hydraulic conductivity corresponding to volumetric water content; K_{sat} is the saturated hydraulic conductivity; x is the integral dummy variable for water content; and θ_{res} represents the residual volumetric water content.

The hydraulic head difference caused by tidal level fluctuations outside the slope drives the internal seepage of the slope; the groundwater table within the slope is defined as the phreatic line. The soil mass below the phreatic line is in a saturated state, whereas the soil mass above the phreatic line is in an unsaturated state. Both pore water pressure and pore air pressure exist in the voids of unsaturated soil, and the difference between pore water pressure and pore air pressure is characterized as matric suction.

2.2. Model Establishment

According to the literature [3,22], the far-field groundwater level of coastal slopes is nearly equivalent to the elevation of the average sea level. In this study, the initial groundwater level of the coastal slope was set to match the average sea level, and the left far-field boundary is placed sufficiently far from the slope to avoid boundary effects. A numerical slope model was thereby established to verify the theoretical calculation results of this research. The tidal water level is applied to the slope surface as a time-dependent Dirichlet (hydraulic head) boundary. During simulation, the boundary hydraulic head is updated in real time according to the semi-diurnal tidal variation, directly providing dynamic external hydraulic conditions for the saturated–unsaturated seepage governing equation. A two-dimensional numerical representation of the coastal slope was established via the finite element software GeoStudio. The model adopted a uniform mesh of 1 m, with a total of 2108 elements and 2207 nodes. The mesh quality satisfied the Mohr–Coulomb strength criterion and the associated flow rule. Fixed displacement boundaries were applied at the bottom and both sides of the model [17,24], as depicted in Figure 1.

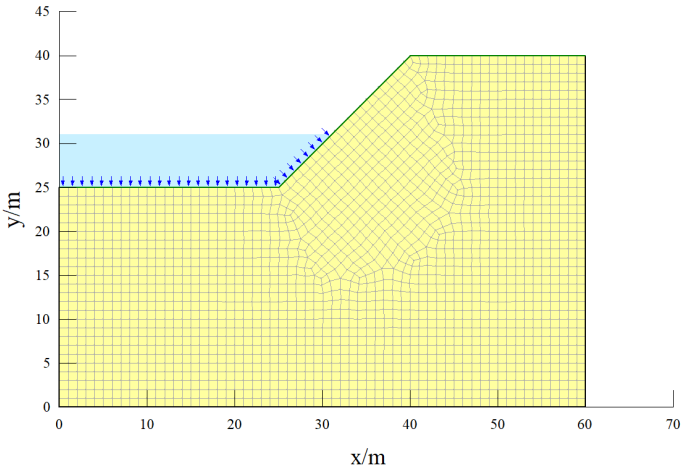


Figure 1. GeoStudio modeling.

2.3. Parameter Selection

The slope model in this study was defined as a homogeneous soil medium; this model can reflect the core mechanism by which tidal level fluctuations influence the seepage characteristics and stability of coastal slopes, and the conclusions are universally applicable to conventional coastal slopes [6,22]. However, the model does not consider the hysteresis of the soil-water characteristic curve (SWCC), which may exert a certain influence on the calculation of pore-water pressure and the fluctuation amplitude of the safety factor. This issue will be addressed in future research. The initial parameters were set as follows: total unit weight γ = 20 kN/m^3, unit weight of water γ_w = 9.8 kN/m^3, cohesion c = 20 kPa, internal friction angle $\varphi = 25^\circ$, mean sea level h_0/H = 0.4, tidal amplitude A = 1 m, elastic modulus E = 10 MPa, Poisson's ratio ν = 0.33, and saturated hydraulic conductivity $k_s = 1 \times 10^{-6}$ m/s. Considering the influences of soil parameters, tidal range and mean sea level on coastal slope stability, comparative parameter analyses are conducted with various values: cohesion c = 20 kPa, 25 kPa, 30 kPa; internal friction angle $\varphi = 25^\circ$, 28°, 30°; mean sea level h_0/H = 0.4, 0.5, 0.6; and tidal range A = 1 m, 1.5 m, 2 m, to investigate the variation laws of coastal slope stability under different parameter conditions. The parameter selection range in this study refers to the research findings of Wang et al. [11] and Kong et al. [25]. By inputting the matric suction and volumetric water content of the soil-water characteristic curve provided by GeoStudio, the F-X model was fitted, and the soil-water characteristic curve and hydraulic conductivity function curve of unsaturated rock and soil mass were obtained (see Figure 2).

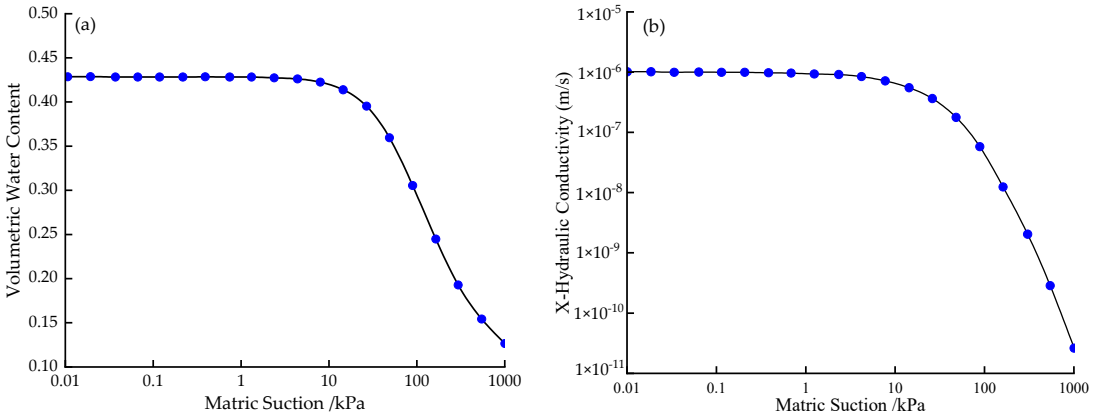


Figure 2. Soil-water characteristic curve and permeability curve: (**a**) Soil-water characteristic curve; (**b**) Permeability curve.

2.4. Case Setup

This study adopts a simplified two-dimensional ideal model to analyze slope stability under semi-diurnal tidal action. The current model does not consider wave erosion or other complex dynamic loads. Wave erosion is a surface mechanical scouring process involving hydrodynamic action, sediment transport, and slope toe erosion, which is fundamentally different from the internal seepage characteristics induced by tidal level changes. This study aims to reveal the fundamental mechanism of groundwater flow driven by tidal fluctuations. Accordingly, the conclusions of this paper are only applicable to ideal tidal conditions and can serve as a fundamental reference. To explore the distribution pattern of the groundwater table within coastal slopes under tidal level oscillations, and to evaluate the impact of tidal elevations on the slope's groundwater regime at various tidal time instants, a case characterized by h_0/H = 0.4 and A = 1 m is taken as a typical illustrative example. The simulation configuration is established as follows: the overall elevation of the slope system is 40 m, with the actual slope height H set to 15 m, and the slope angle β = 45°; the initial hydraulic head is assigned to the mean sea level h_0, which is situated 6 m above the slope toe. The duration of tidal water level variation is 1 day, and the water level increments are stored in 24 steps. The tidal water level elevation function adopts a semi-diurnal tidal mode, as shown in Figure 3 below.

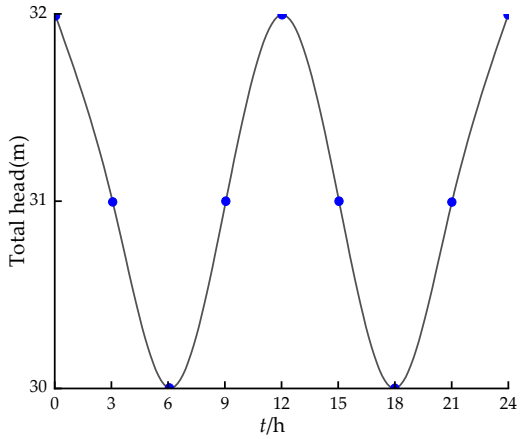


Figure 3. Variation in tidal water level within 24 h.

When simulating the groundwater level of coastal slopes using the SEEP module in GeoStudio software, steady-state seepage analysis is first performed to calculate the seepage field under the initial water level, followed by transient seepage analysis to examine the seepage field under varying water levels, thereby obtaining the phreatic line of the coastal slope that varies with tidal rise and fall. The calculated results are imported into the SLOPE module, where the entry and exit points of the slip surface are defined according to the theoretical calculations in this study, and the stability analysis of the coastal slope is then conducted.

2.5. Safety Factor Calculation

In slope stability evaluation, the strength reduction factor serves as the central component of the limit equilibrium methodology. Its core principle entails gradually decreasing the shear strength attributes of the soil and rock mass comprising the slope, thereby propelling the slope system towards a state of critical balance. The safety factor is specified as the proportion of the original shear strength of the slope relative to the diminished shear strength at which the slope transitions into a condition of impending failure.

The distribution of groundwater level in coastal slopes under tidal level variations is simulated using the SEEP module, and the results are imported into the SLOPE module

for calculation using the Morgenstern–Price method. The detailed calculation flow is illustrated in Figure 4. The Morgenstern–Price method introduces a functional assumption for the direction of inter-slice forces. By iteration, it simultaneously solves for the safety factor and a scaling factor λ of this function, while satisfying both force equilibrium and moment equilibrium for all slices. It is applicable to any complex slip surface and soil layer conditions, representing an advanced analysis method in SLOPE/W.

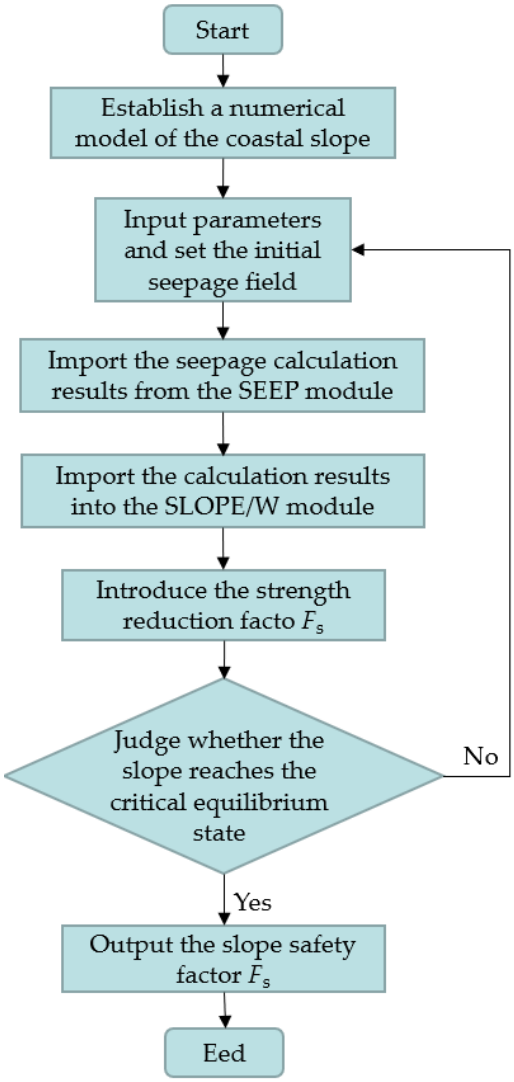


Figure 4. Calculation flow of safety factor.

3. Analysis of Numerical Simulation Results

3.1. Variation Law of the Phreatic Line

Figure 5 illustrates the distribution of the phreatic surface within the slope over a 24-h tidal cycle, commencing from the mean sea level. It can be seen from the phreatic line distribution at each moment in the figure that with the tidal fluctuation, the phreatic line inside the slope rises as the water level rises and falls as the water level drops. The variation in the phreatic line exhibits a hysteresis effect and the same periodicity as the water level variation. There is a limit to the variation in the phreatic line: when the tide reaches the late flood stage at t = 0 h, namely the peak external water level, the phreatic line also reaches its upper bound; when the tide reaches the late ebb stage at t = 6 h, namely the lowest external water level, the phreatic line reaches its lower bound.

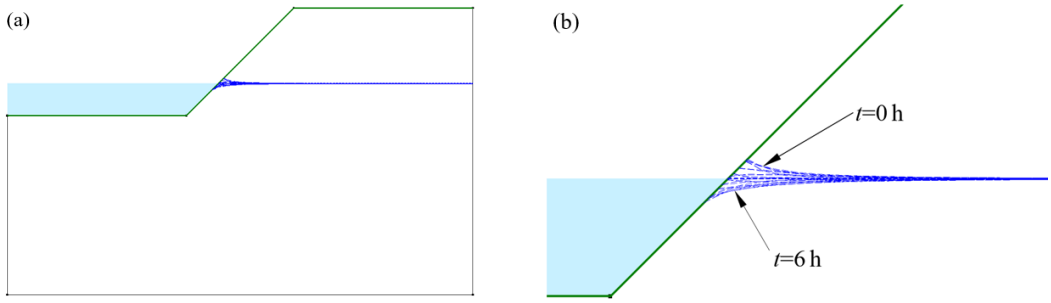


Figure 5. Variation in the phreatic line within 24 h: (**a**) Overall view; (**b**) partial enlarged view.

3.2. Variation Law of Pore Water Pressure

3.2.1. Influence of Mean Sea Level Height

Based on the distribution of the phreatic line, three time points are considered particularly important for the coastal slope: the late flood stage at t = 0 h, the mean sea level period at t = 3 h, and the late ebb stage at t = 6 h. Given that the mean sea level elevation affects the groundwater table distribution within the slope, three scenarios (h_0/H = 0.4, 0.5, and 0.6) are selected for comparative analysis. As depicted in Figure 6, the pore water pressure along the slope surface increases monotonically with the rise in the mean sea level. During tidal level fluctuations, the pore water pressure in the slope's near-surface region undergoes notable changes, whereas the variation is minimal in the zone far from the slope surface; the amplitude of pore water pressure variation in the slope surface region synchronizes with the tidal level oscillations. When the tidal level fluctuates, a hydraulic head gradient is formed across the slope boundary. Taking the ebb tide interval from t = 0 h to t = 6 h as an example, as the water level recedes, the seepage vectors point outward from the slope, driving water discharge from the slope interior to the exterior, which lowers the internal groundwater table and gradually dissipates the pore water pressure. Due to the seepage hysteresis phenomenon, the speed at which pore water pressure dissipates inside the slope falls behind the speed of water level reduction, maintaining the pore water pressure in the area far from the slope surface at a high level. This generates a seepage gradient difference that elevates the risk of slope instability.

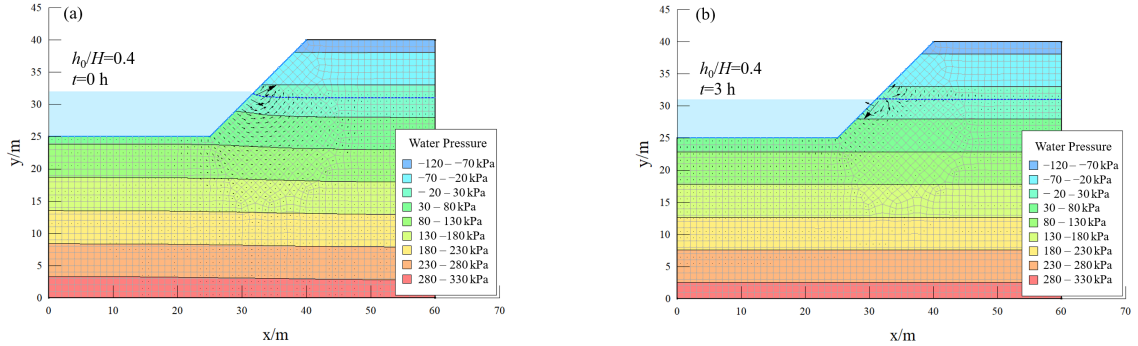


Figure 6. *Cont.*

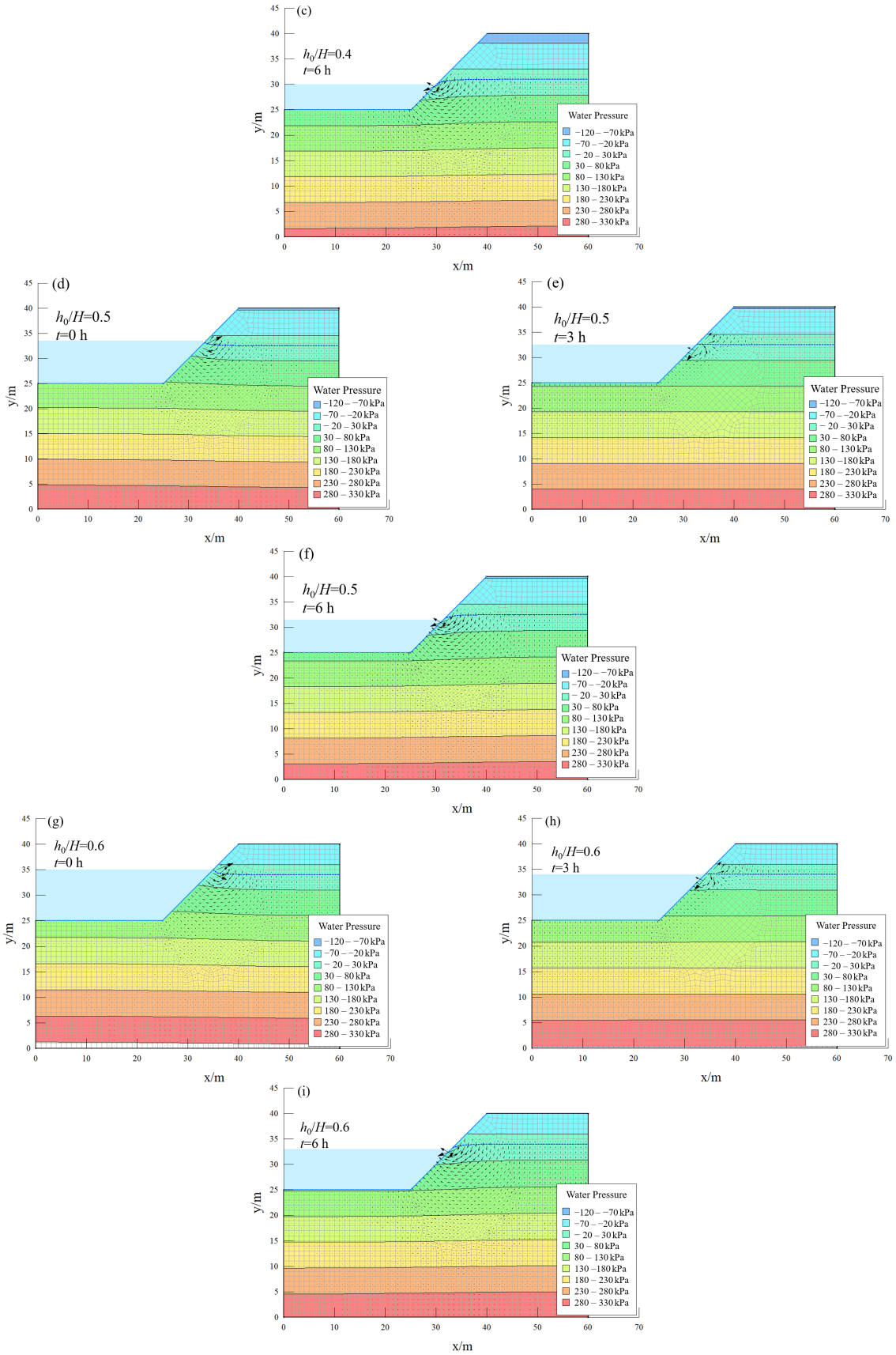


Figure 6. Seepage vectors and pore water pressure distribution of coastal slope under different mean sea levels: (**a**) h_0/H = 0.4, t = 0 h; (**b**) h_0/H = 0.4, t = 3 h; (**c**) h_0/H = 0.4, t = 6 h; (**d**) h_0/H = 0.5, t = 0 h; (**e**) h_0/H = 0.5, t = 3 h; (**f**) h_0/H = 0.5, t = 6 h; (**g**) h_0/H = 0.6, t = 0 h; (**h**) h_0/H = 0.6, t = 3 h; (**i**) h_0/H = 0.6, t = 6 h.

It can be seen from Figure 7 that under the time-history effect of semi-diurnal tides, the influence of different mean sea levels on the safety factor F_s of coastal slopes shows a periodic fluctuation pattern of "first decreasing and then increasing". F_s reaches its peak at the late flood stage t = 0 h and drops to the valley at the late ebb stage t = 6 h, which is highly consistent with the variation characteristics of the semi-diurnal tidal level. Meanwhile, as h_0/H increases, the overall stability of the coastal slope improves, but the fluctuation amplitude of F_s increases significantly, and the relative difference in the safety factor between the late flood and ebb stages also expands accordingly. For example, when h_0/H = 0.4, the relative difference is 8.60%; when h_0/H = 0.6, the relative difference increases to 11.86%. This indicates that the variations in coastal slope stability induced by different mean sea levels are relatively small. Nevertheless, such minor variations remain of great significance in practical coastal slope engineering. Although the relative variation in the safety factor increases slightly, tidal effects act repeatedly and cyclically over a long period and accumulate continuously. This further induces soil fatigue, strength degradation and progressive failure, keeping the slope in a critical unstable state for a long time. Such subtle variations are more dangerous, concealed and difficult to monitor and forecast in practical engineering applications, posing more significant potential threats to the long-term service safety of coastal slopes.

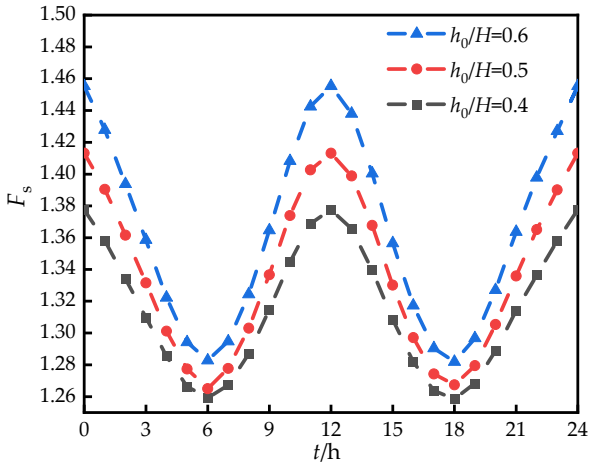


Figure 7. Variation law of safety factor of coastal slopes with mean sea level.

Figure 8 presents the safety factor contours and the locations of the critical slip surfaces of the slope at three key time instants (t = 0 h, t = 3 h, and t = 6 h) under three mean sea level ratios (h_0/H = 0.4, 0.5, and 0.6). It can be seen from the figure that the overall safety factor of the slope gradually increases with the rise in the mean sea level. The safety factor isolines decrease gradually from the slope crest to the slope toe, and the low-value zones are concentrated in the slope toe and the shallow surface area of the slope. During the dynamic change in tidal water level, the spatial position, depth and morphology of the slip surface remain basically stable, except that the potential failure range expands slightly at the end of the falling tide (t = 6 h), with a longer failure width at the slope crest and a slightly increased burial depth of the slip surface. The results indicate that the mean sea level height affects the magnitude and fluctuation amplitude of the safety factor mainly by altering the pore-water pressure and stress state within the slope, without causing obvious migration of the slip surface, which reflects the concealment of the tidal effect on the stability of coastal slopes.

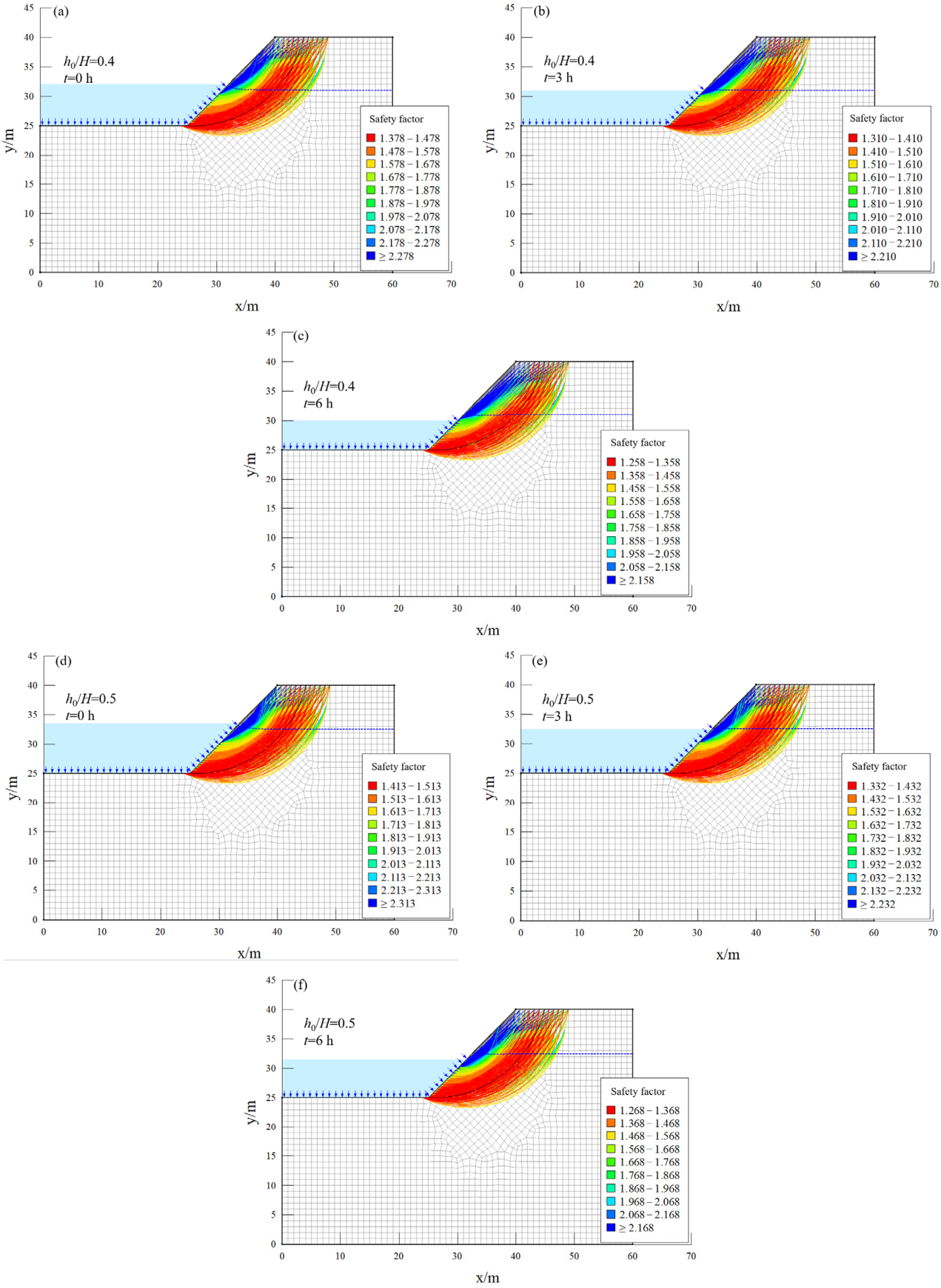


Figure 8. *Cont.*

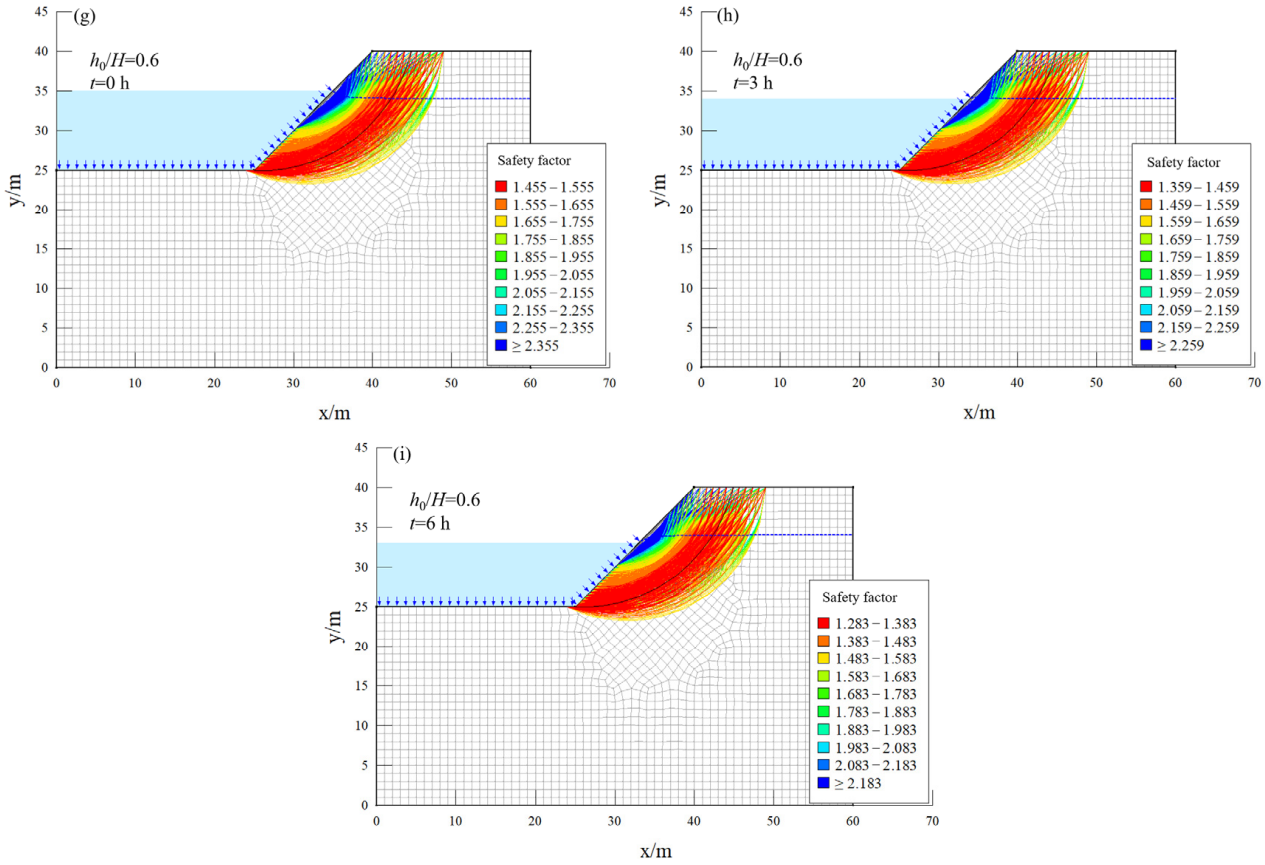


Figure 8. Critical slip surfaces of coastal slopes at three key time points under different mean sea levels: (**a**) h_0/H = 0.4, t = 0 h; (**b**) h_0/H = 0.4, t = 3 h; (**c**) h_0/H = 0.4, t = 6 h; (**d**) h_0/H = 0.5, t = 0 h; (**e**) h_0/H = 0.5, t = 3 h; (**f**) h_0/H = 0.5, t = 6 h; (**g**) h_0/H = 0.6, t = 0 h; (**h**) h_0/H = 0.6, t = 3 h; (**i**) h_0/H = 0.6, t = 6 h.

3.2.2. Effect of Tidal Range

Tidal range originates from the periodic oscillation of tidal water levels, and its magnitude governs the amplitude of the hydraulic head gradient across the slope boundary, which exerts a pronounced impact on the groundwater table distribution, seepage field evolution, and stability characteristics of coastal slopes. Accordingly, three scenarios with tidal amplitudes A = 1 m, 1.5 m, and 2 m are selected for comparative investigation. As illustrated in Figure 9, a larger tidal range correlates with a more pronounced fluctuation amplitude of the pore water pressure on the slope surface, and both the spatial extent and intensity of tidal disturbance to the internal seepage field are significantly amplified. During tidal level oscillations, the pore water pressure response remains concentrated in the near-surface zone, while the deep soil mass is comparatively less affected. In the ebb tide phase (t = 0 h ∼ t = 6 h), a larger tidal range leads to a more prominent transient hydraulic head gradient between the slope interior and exterior, a stronger driving force for outward seepage, and a more rapid dissipation of pore water pressure. Under the effect of seepage hysteresis, a steeper seepage gradient difference is formed inside the slope, and the inhomogeneous distribution of effective stress becomes more prominent. Consequently, the larger the tidal range is, the more obvious the stability degradation of the slope at the late ebb stage t = 6 h, and the higher the instability risk.

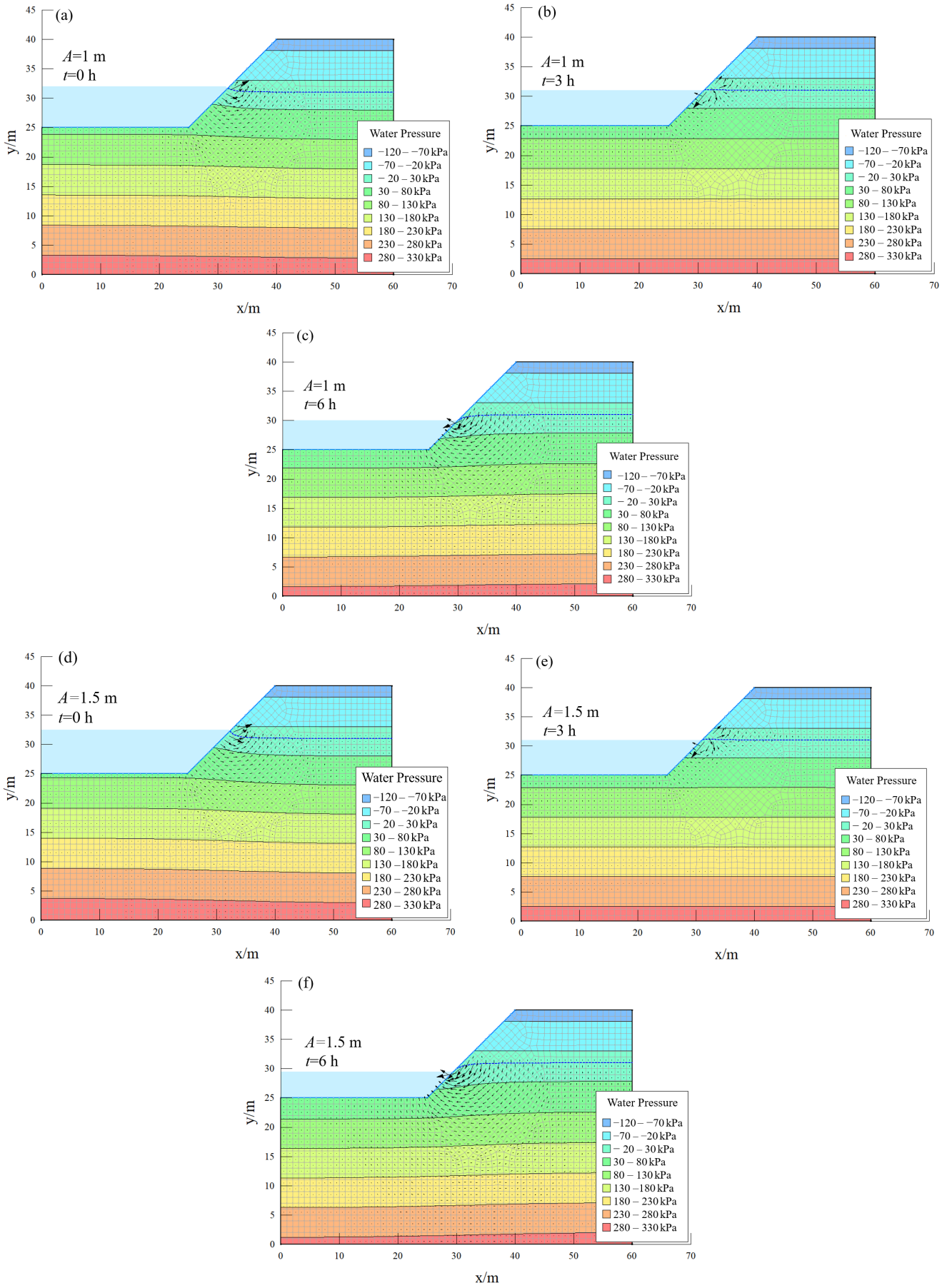


Figure 9. *Cont.*

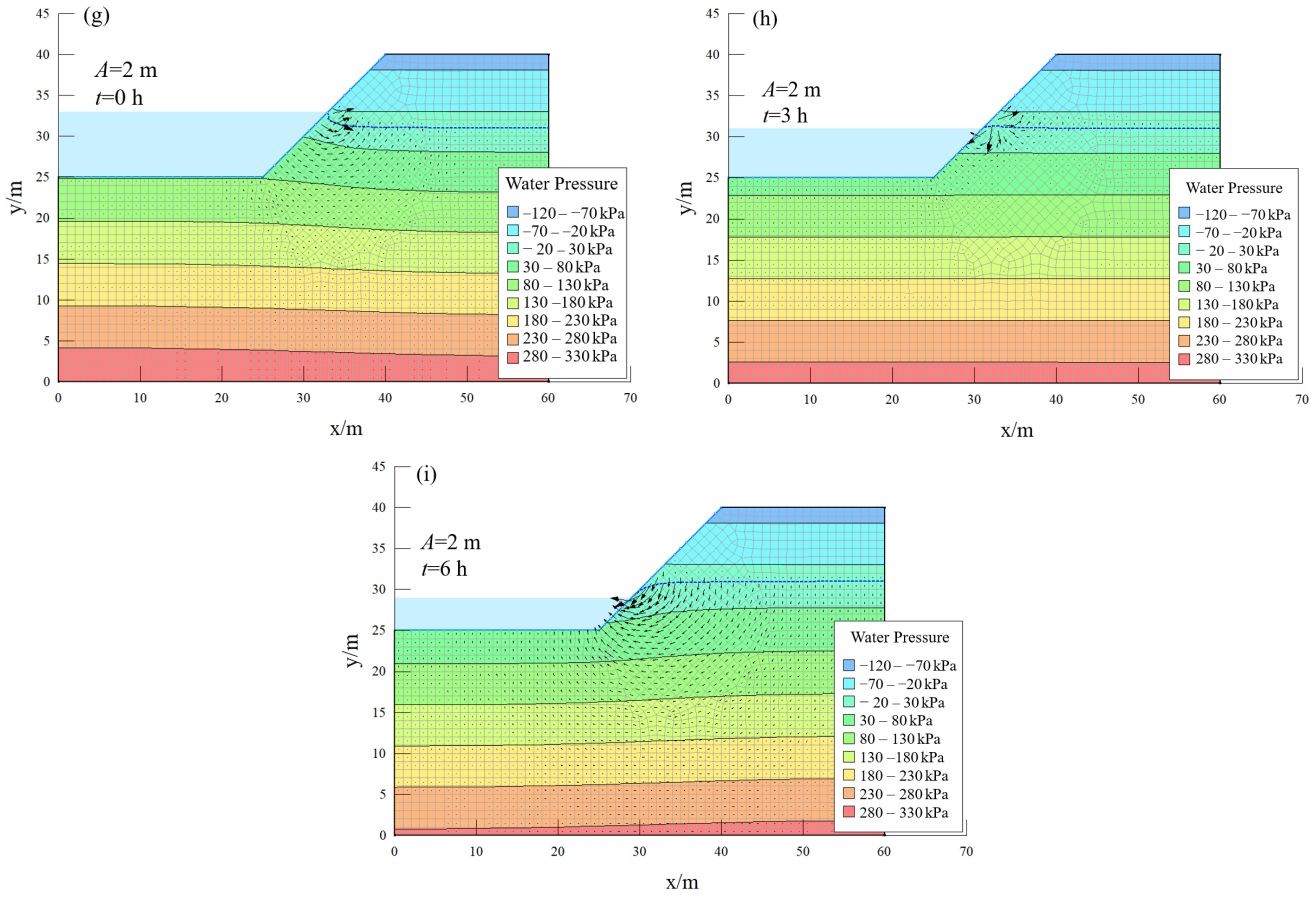


Figure 9. Seepage vectors and pore water pressure distribution of coastal slope under different tidal ranges: (**a**) A = 1 m, t = 0 h; (**b**) A = 1 m, t = 3 h; (**c**) A = 1 m, t = 6 h; (**d**) A = 1.5 m, t = 0 h; (**e**) A = 1.5 m, t = 3 h; (**f**) A = 1.5 m, t = 6 h; (**g**) A = 2 m, t = 0 h; (**h**) A = 2 m, t = 3 h; (**i**) A = 2 m, t = 6 h.

Figure 10 reveals that under various tidal ranges, the slope safety factor F_s exhibits a temporal trend of initial decrease followed by a subsequent increase. With the augmentation of tidal range, the overall magnitude of the safety factor diminishes marginally, while its fluctuation amplitude rises substantially. Specifically, when A = 2 m, the safety factor attains its minimum value at the late ebb stage (t = 6 h). For instance, the relative difference reaches 8.60% for A = 1 m, and this value increases to 16.35% for A = 2 m. It can be seen from Figure 11 the distribution of critical slip surfaces and safety factor contours under different tidal ranges that the spatial position, buried depth and morphology of the critical slip surface of the slope remain basically stable under various tidal range conditions, with no obvious migration as the tidal range increases. The distribution pattern of high and low safety factor zones also shows no significant change. A larger tidal range gives rise to a more pronounced transient hydraulic head difference between the slope interior and exterior, driven by the alternating water level oscillations. This intensifies the uneven dissipation of pore water pressure induced by seepage hysteresis within the slope during the ebb tide phase, consequently resulting in a more significant reduction in the safety factor and an elevated risk of instability. This observation implies that a more substantial water level drop corresponds to a more pronounced variation amplitude in the safety factor of coastal slopes, along with a higher likelihood of instability during the ebb tide phase.

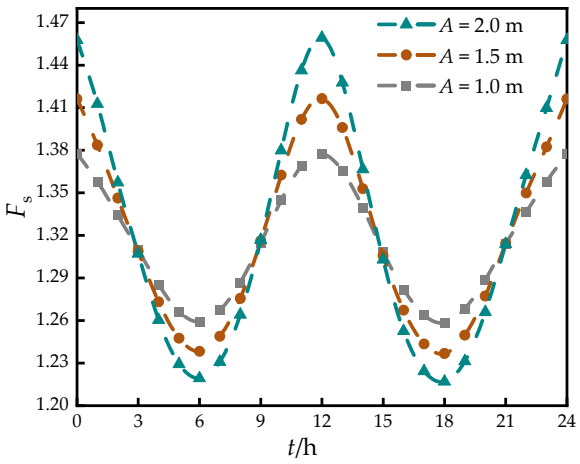


Figure 10. Variation law of safety factor of coastal slopes with tidal range.

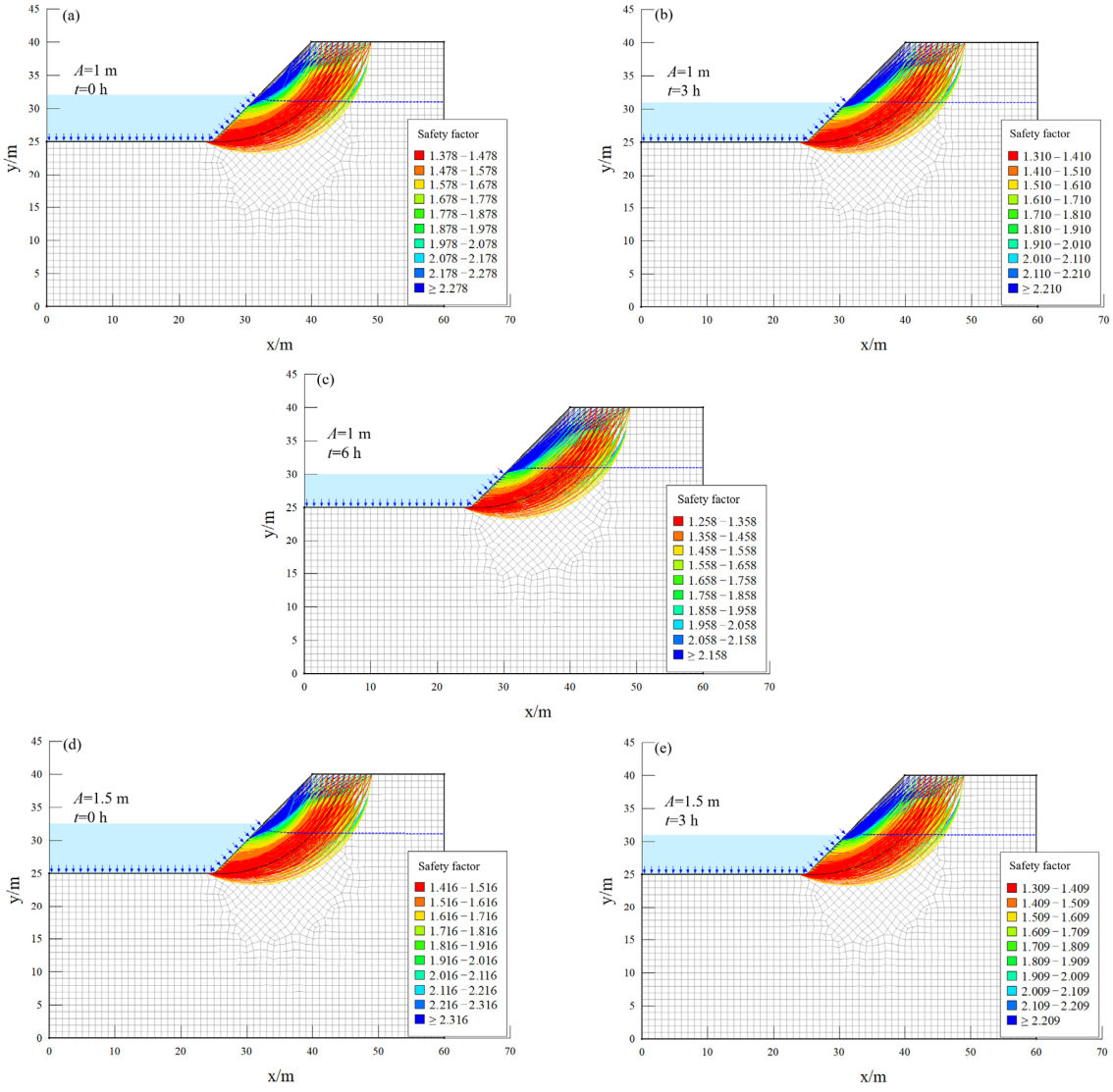


Figure 11. *Cont.*

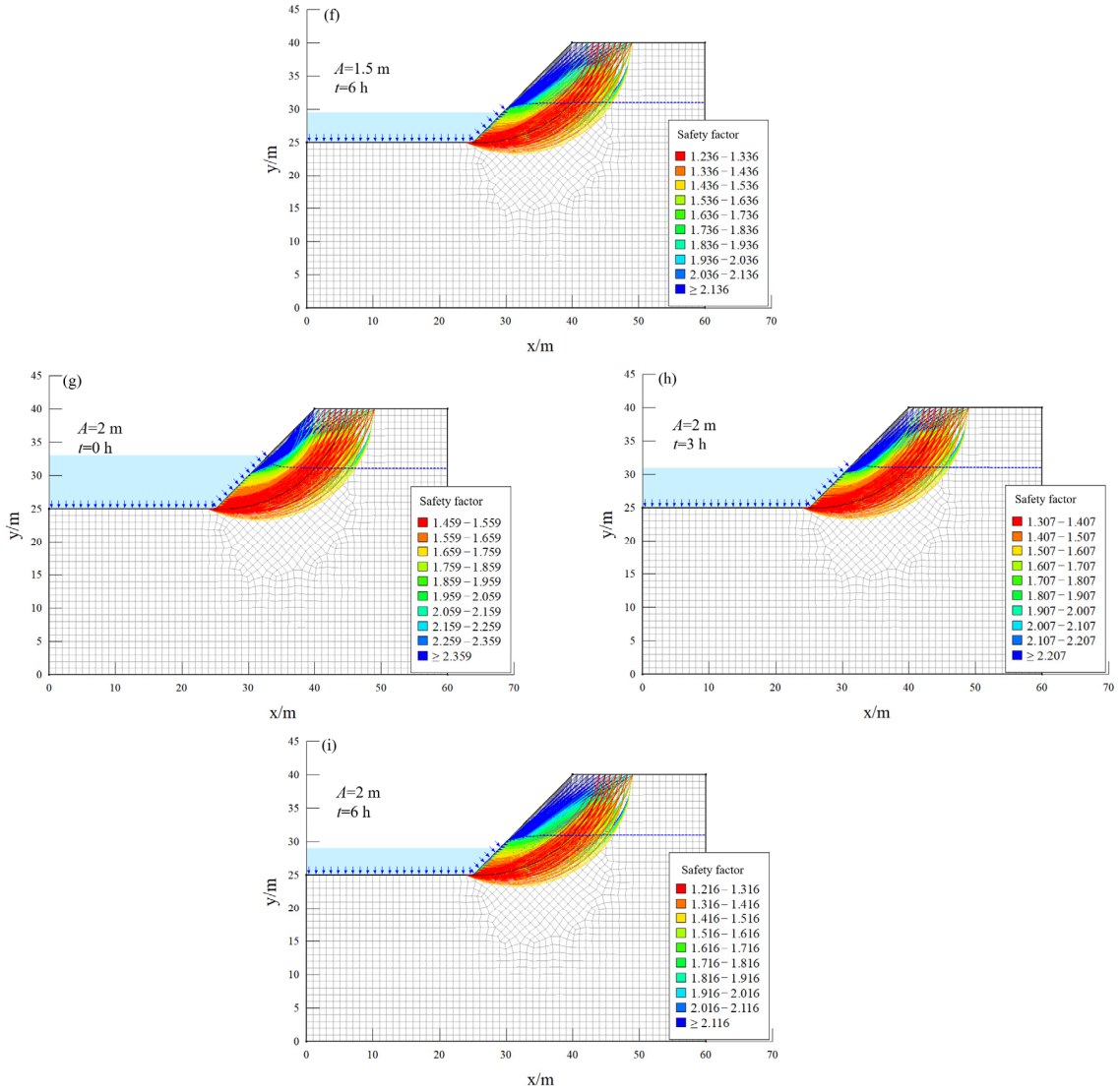


Figure 11. Critical slip surfaces of coastal slopes at three key time points under different tidal ranges: (**a**) A = 1 m, t = 0 h; (**b**) A = 1 m, t = 3 h; (**c**) A = 1 m, t = 6 h; (**d**) A = 1.5 m, t = 0 h; (**e**) A = 1.5 m, t = 3 h; (**f**) A = 1.5 m, t = 6 h; (**g**) A = 2 m, t = 0 h; (**h**) A = 2 m, t = 3 h; (**i**) A = 2 m, t = 6 h.

3.3. Variation Law of Soil Parameters

Figure 12 demonstrates that within a 12 h semi-diurnal tidal cycle, the safety factor F_s of the coastal slope displays a periodic trend of initial drop followed by subsequent rebound, with cohesion c and internal friction angle φ varied independently. A comparative analysis of the two sets of curves reveals that the internal friction angle φ exerts a more pronounced influence on both the magnitude and fluctuation amplitude of the safety factor. F_s increases overall with a rise in φ and exhibits a larger fluctuation amplitude. In contrast, increasing the cohesion c can also raise F_s, but it reduces the relative difference in the safety factor between the late flood and ebb stages and tends to smooth out the fluctuations. According to the data patterns, a larger φ leads to a slight increase in the safety factor difference between the two moments, while a larger c results in a decrease in the difference. This indicates that the two shear strength indices have different effects on slope stability: increasing the internal friction angle can enhance stability but amplifies the tidal effect, whereas increasing cohesion improves stability while weakening fluctuations and reducing the risk of instability during ebb tide. The collaborative optimization of both indices can more effectively enhance the overall stability of coastal slopes.

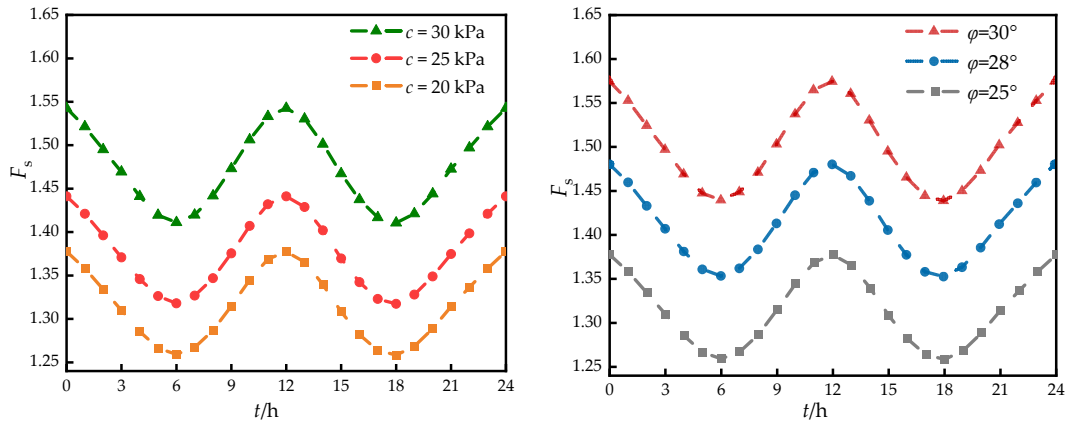


Figure 12. Variation law of safety factor of coastal slopes with shear strength parameters.

Figures 13 and 14 compare the effects of cohesion c and internal friction angle φ on the safety factor distribution and critical slip surface locations of coastal slopes, respectively. The results show that increasing both cohesion and internal friction angle can significantly improve the overall safety factor of the slope, expand the range of high-value zones, and reduce the proportion of low-value zones, which are mainly concentrated at the slope base and the deep region of the slope surface. Meanwhile, the spatial position, buried depth, morphology, and failure range of the critical slip surface remain unchanged without obvious migration, and the slip surface development position stays stable. This indicates that coastal slopes are more likely to reach a critical state and trigger instability at the slope base and deep slope surface under tidal effects. It further verifies the concealment and abruptness of slope failure induced by tidal action. This study clarifies the concealed disaster-causing mechanism of slope instability under tidal effects, which can provide a key risk prediction basis and standardized technical support for disaster-resistant design of coastal slopes, dikes, and other projects in southeast coastal areas.

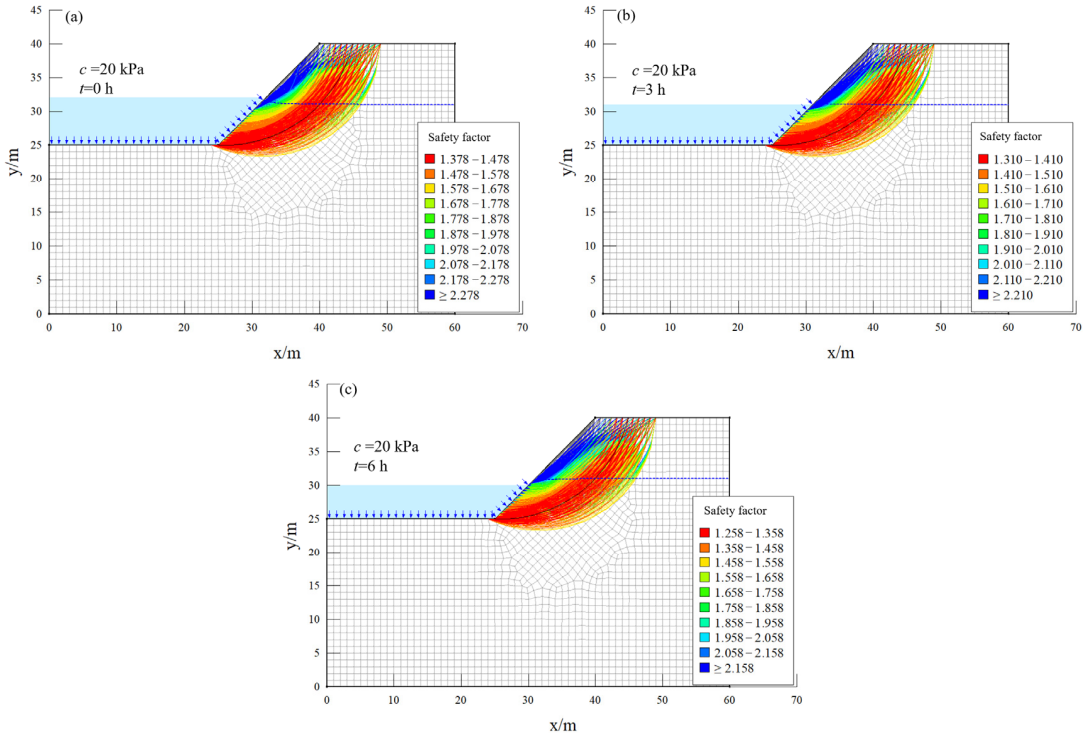


Figure 13. *Cont.*

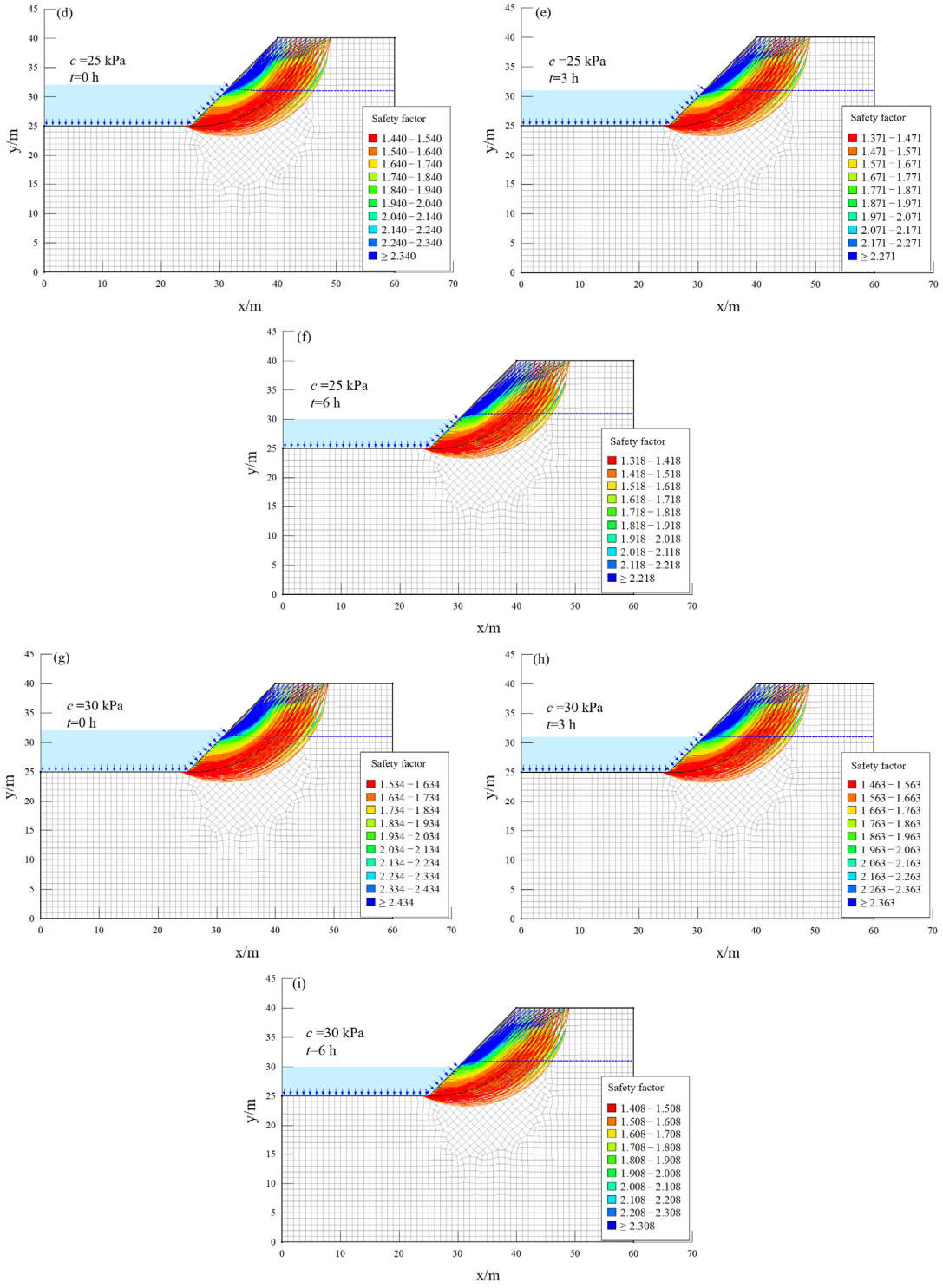


Figure 13. Critical slip surfaces of coastal slopes at three key time points under different cohesion values: (**a**) c = 20 kPa, t = 0 h; (**b**) c = 20 kPa, t = 3 h; (**c**) c = 20 kPa, t = 6 h; (**d**) c = 25 kPa, t = 0 h; (**e**) c = 25 kPa, t = 3 h; (**f**) c = 25 kPa, t = 6 h; (**g**) c = 30 kPa, t = 0 h; (**h**) c = 30 kPa, t = 3 h; (**i**) c = 30 kPa, t = 6 h.

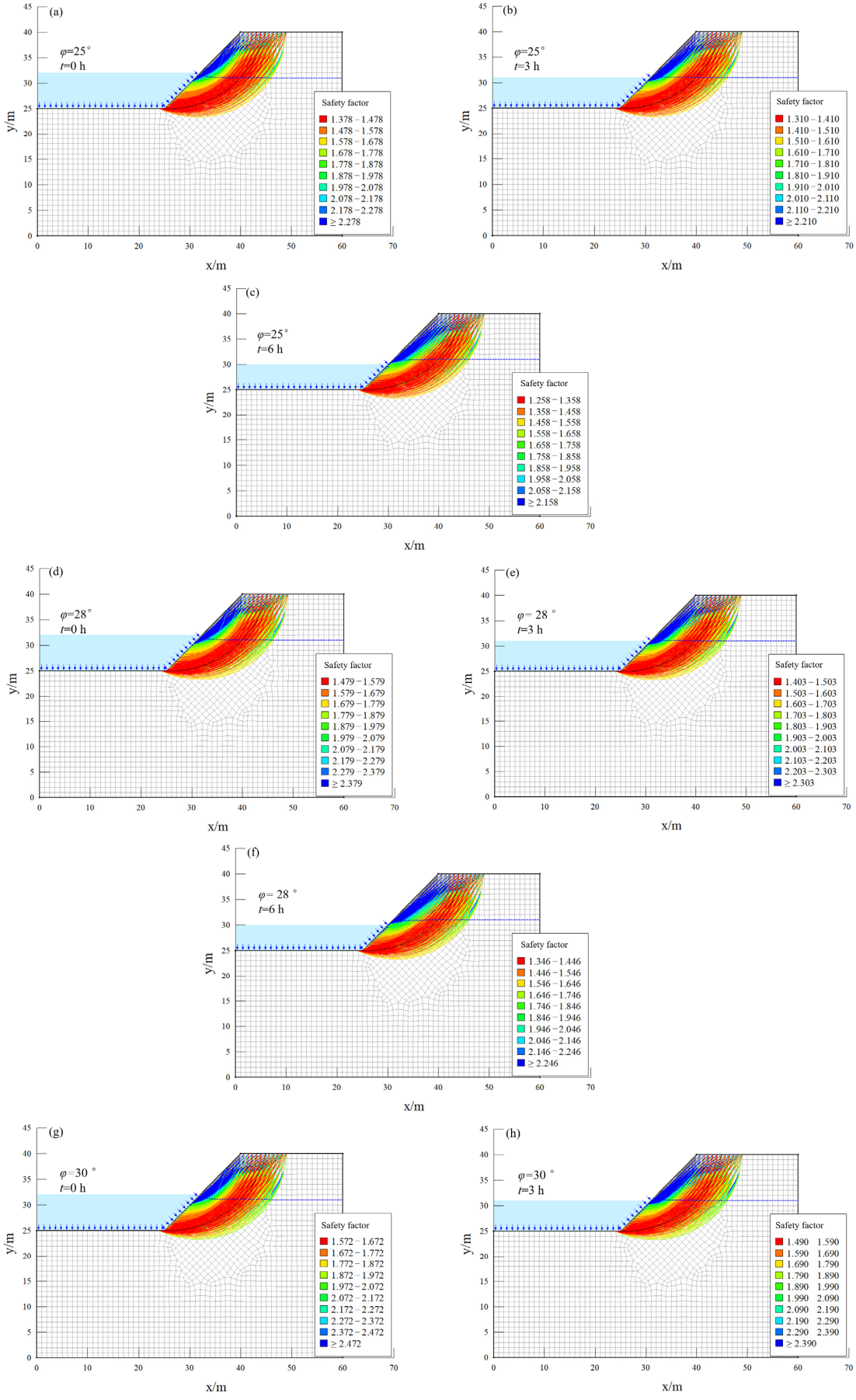


Figure 14. *Cont*.

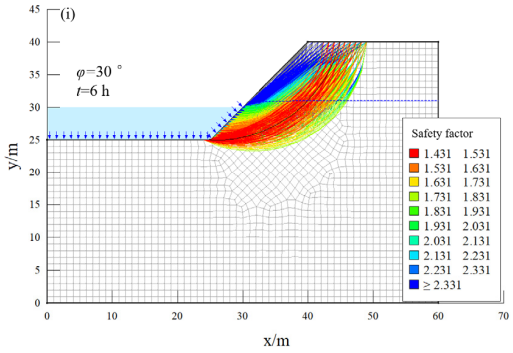


Figure 14. Critical slip surfaces of coastal slopes at three key time points under different internal friction angles: (**a**) c = 25°, t = 0 h; (**b**) c = 25°, t = 3 h; (**c**) c = 25°, t = 6 h; (**d**) c = 28°, t = 0 h; (**e**) c = 28°, t = 3 h; (**f**) c = 28°, t = 6 h; (**g**) c = 30°, t = 0 h; (**h**) c = 30°, t = 3 h; (**i**) c = 30°, t = 6 h.

4. Theoretical Analysis Model for Coastal Slope Stability

In the preceding section, numerical experiments were conducted to examine the seepage field characteristics and stability behavior of coastal slopes subjected to tidal level oscillations. Through these simulations, the temporal evolution patterns of the internal phreatic surface and pore water pressure at distinct time instants t were successfully identified and analyzed. Based on these findings from numerical simulations in this section, the initial conditions of the analytical solution and the numerical model are kept consistent, and a theoretical analysis model for coastal slope stability verifies the scientific rigor of the analytical method and the validity of the computational results in this study by comparing the theoretical calculations with the numerical simulation outcomes.

4.1. Analytical Solution of Groundwater Level Distribution in Slope Under Time-History Effect of Semi-Diurnal Tide

According to the research study [26], a semi-diurnal tide-dominated mode is adopted for the tidal level time-history function in this paper, ignoring minor tidal constituents. The expression of the semi-diurnal tidal level is given as:

$$h_t(t) = h_0 + A \cdot \cos(\frac{2\pi}{T}t) \tag{4}$$

where h_1 is the sea level height at time t, h_0 is the mean sea level, A is the tidal range, t is the time, and the semi-diurnal tidal period T = 12 h.

Under tidal action, the flow in rigid porous media is assumed to be uniform, isothermal and incompressible, and the medium is constrained at the surface without mass loss. As shown in Figure 15, H denotes the slope height and β denotes the slope angle. The slope slides clockwise around point O at the angular velocity ω. The distances from point O to points A and C are r_0 and r_h respectively, and the angles between OA, OB, OC and the horizontal direction are θ_0, θ_B and θ_h respectively.

Under tidal action, Nielsen [27] derived an analytical expression for the groundwater level distribution inside coastal slopes. This analytical solution takes the projection of the intersection point between the external mean sea level and the slope surface onto the horizontal line at the slope base as the coordinate origin, and can accurately describe the variation characteristics of the groundwater level in coastal slopes under tidal influence. In this paper, the coordinate origin of the analytical solution for water level distribution is set at the slope toe C, and the corresponding expression is given as

$$\begin{aligned} h(x,t) &= D + A\mathrm{e}^{(-\frac{x+h_0\cot\beta}{L})}\cos(\frac{2\pi t}{T} - \frac{x+h_0\cot\beta}{L}) \\ &+ \frac{A^2\cot\beta}{L}\{\frac{1}{2} + \frac{1}{\sqrt{2}}\mathrm{e}^{\sqrt{2}(-\frac{x+h_0\cot\beta}{L})}\cos[\frac{4\pi t}{T} + \sqrt{2}(-\frac{x+h_0\cot\beta}{L}) + \frac{\pi}{4}]\} \end{aligned} \tag{5}$$

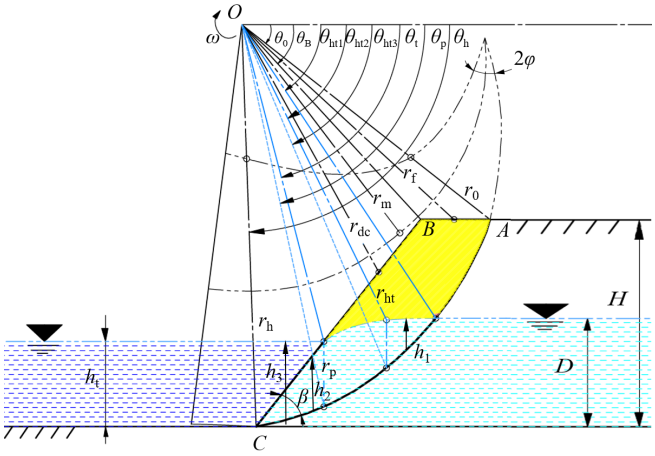


Figure 15. Stability analysis model of coastal slopes under semi-diurnal tide effect.

In the above expression, $L = \sqrt{\frac{ksDT}{\pi n_e}}$, D denotes the elevation of the far-field static water table within the slope, k_s represents the hydraulic conductivity of the slope soil, and n_e stands for the effective porosity.

$$\begin{cases} x = r_{ht}\cos\theta - r_h\cos\theta_h \\ h = r_h\sin\theta_h - r_{ht}\sin\theta \end{cases} \tag{6}$$

Substituting Equation (6) into Equation (5) yields the implicit analytical solution for the internal water level distribution $r_{ht}(\theta, t)$ within the slope, as follows:

$$\begin{aligned} r_h\sin\theta_h - r_{ht}\sin\theta &= D + A\mathrm{e}^{(-\frac{r_{ht}\cos\theta - r_h\cos\theta_h + h_0\cot\beta}{L})} \\ &\times\cos(\frac{2\pi t}{T} - \frac{r_{ht}\cos\theta - r_h\cos\theta_h + h_0\cot\beta}{L}) \\ &+ \frac{A^2\cot\beta}{L}\{\frac{1}{2} + \frac{1}{\sqrt{2}}\mathrm{e}^{\sqrt{2}(-\frac{r_{ht}\cos\theta - r_h\cos\theta_h + h_0\cot\beta}{L})} \\ &\cdot\cos[\frac{4\pi t}{T} + \sqrt{2}(-\frac{r_{ht}\cos\theta - r_h\cos\theta_h + h_0\cot\beta}{L}) + \frac{\pi}{4}]\} \end{aligned} \tag{7}$$

Slope surface *BC* lies on the symmetry plane of the failure mass. The distance from point *O* to an arbitrary point on *BC* is denoted as r_{dc}, and its expression is given as:

$$r_{dc} = \frac{r_h\sin(\theta_h + \beta)}{\sin(\theta + \beta)} \tag{8}$$

4.2. External Force Power and Internal Energy Dissipation

(1) Gravity Power

The expression for the gravity power $\dot{W}_\gamma$ acting on the block above the phreatic surface is given as

$$\begin{aligned} \dot{W}_\gamma &= \{\int_{\theta_0}^{\theta_h}\frac{2}{3}\omega r\cos\theta\cdot\frac{1}{2}\gamma r^2\mathrm{d}\theta - \int_{\theta_0}^{\theta_B}\frac{2}{3}\omega r_f\cos\theta\cdot\frac{1}{2}\gamma r_f^2\mathrm{d}\theta - \int_{\theta_B}^{\theta_h}\frac{2}{3}\omega r_{dc}\cos\theta\cdot\frac{1}{2}\gamma r_{dc}^2\mathrm{d}\theta \\ &-[\int_{\theta_{ht1}}^{\theta_h}\frac{2}{3}\omega r\cos\theta\cdot\frac{1}{2}\gamma r^2\mathrm{d}\theta - \int_{\theta_{ht1}}^{\theta_{ht2}}\frac{2}{3}\omega r_{ht}\cos\theta\cdot\frac{1}{2}\gamma r_{ht}^2\mathrm{d}\theta - \int_{\theta_{ht2}}^{\theta_h}\frac{2}{3}\omega r_{dc}\cos\theta\cdot\frac{1}{2}\gamma r_{dc}^2\mathrm{d}\theta]\} \end{aligned} \tag{9}$$

In the above equation, γ is the unit weight of soil. To clarify the spatial intersection relationships among the internal groundwater distribution, the slope surface water level, the failure surface and the slope face, the polar angles of key intersection points are determined by defining specific geometric conditions. The detailed derivation is presented as follows: ① By setting $r_{\mathrm{ht}}(\theta, t) = r(\theta)$, the polar angle corresponding to the intersection between the internal groundwater distribution r_{ht} and the failure surface is obtained and denoted as θ_{ht1}. ② By setting $r_{\mathrm{ht}}(\theta, t) = rdc(\theta)$ the polar angle corresponding to the intersection between the internal groundwater distribution r_{ht} and the slope surface is derived and denoted as θ_{ht2}.

The distance from point O to an arbitrary point on the top width AB of the slope is denoted as r_{f}, and its expression is given as:

$$r_{\mathrm{f}} = r_0 \frac{\sin\theta_0}{\sin\theta} \tag{10}$$

The expression for the gravity power $\dot{W}_{\gamma\prime}$, acting on the soil mass below the phreatic surface is given as:

$$\begin{aligned} \dot{W}_{\gamma\prime} = \{ & \int_{\theta_{\mathrm{ht1}}}^{\theta_{\mathrm{h}}} \frac{2}{3}\omega r\cos\theta \cdot \frac{1}{2}\gamma' r^2 \mathrm{d}\theta - \int_{\theta_{\mathrm{ht1}}}^{\theta_{\mathrm{ht2}}} \frac{2}{3}\omega r_{\mathrm{ht}}\cos\theta \cdot \frac{1}{2}\gamma' r_{\mathrm{ht}}^2 \mathrm{d}\theta \\ & - \int_{\theta_{\mathrm{ht2}}}^{\theta_{\mathrm{h}}} \frac{2}{3}\omega r_{\mathrm{dc}}\cos\theta \cdot \frac{1}{2}\gamma' r_{\mathrm{dc}}^2 \mathrm{d}\theta \} \end{aligned} \tag{11}$$

where γ' is the buoyant unit weight of soil.

(2) Power Water Power Inside the Slope

The expression for the pore water pressure power $\dot{W}_{\mathrm{w}}$ under tidal action is given as:

$$\dot{W}_{\mathrm{w}} = \gamma_{\mathrm{w}} r_0^2 \omega \tan\varphi \{ \int_{\theta_{\mathrm{ht1}}}^{\theta_{\mathrm{ht3}}} h_1 \mathrm{e}^{2(\theta-\theta_0)\tan\varphi} \mathrm{d}\theta + \int_{\theta_{\mathrm{ht3}}}^{\theta_{\mathrm{p}}} h_2 \mathrm{e}^{2(\theta-\theta_0)\tan\varphi} \mathrm{d}\theta + \int_{\theta_{\mathrm{p}}}^{\theta_{\mathrm{h}}} h_3 \mathrm{e}^{2(\theta-\theta_0)\tan\varphi} \mathrm{d}\theta \} \tag{12}$$

The specific derivation of the parameters in the above equation is as follows: ① By setting $r_{\mathrm{h}} \cdot \sin\theta_{\mathrm{h}} - r_{\mathrm{dc}} \cdot \sin\theta = h_{\mathrm{t}}$, the polar angle of the intersection point between the coastal water level r_{ht} and the slope surface is obtained, denoted as θ_{t}. A perpendicular line to $r(\theta)$ is drawn at this intersection point. ② By setting $\frac{r_{\mathrm{h}}\sin(\theta_{\mathrm{h}}+\beta)\cos\theta_{\mathrm{t}}}{\sin(\theta_{\mathrm{t}}+\beta)\cos\theta} = r(\theta)$, the polar angle of the perpendicular line is obtained, denoted as θ_{p}. The perpendicular line to the failure surface drawn from the intersection point between the internal groundwater level distribution r_{ht} and the slope surface is defined as r_{p}, $r_{\mathrm{p}} = \frac{r_{\mathrm{h}}\sin(\theta_{\mathrm{h}}+\beta)\cos\theta_{\mathrm{ht2}}}{\sin(\theta_{\mathrm{ht2}}+\beta)\cos\theta}$. ③ By setting $r = r_{\mathrm{p}}(\theta)$, the polar angle of the intersection point between the perpendicular line and the failure surface is obtained, denoted as θ_{ht3}. ④ $h_1 = r\sin\theta - r_{\mathrm{ht}}(\theta_1) \cdot \sin\theta_1$; $h_2 = r \cdot \sin\theta - r_{\mathrm{dc}}(\theta_2) \cdot \sin\theta_2$; $r \cdot \cos\theta = r_{\mathrm{ht}}(\theta_1) \cdot \cos\theta_1$; $r \cdot \cos\theta = r_{\mathrm{dc}}(\theta_2) \cdot \cos(\theta_2)$; $h_3 = r\sin\theta - (r_{\mathrm{h}}\sin\theta_{\mathrm{h}} - h_{\mathrm{t}})$.

(3) Water Level Pressure Power

The expression for the slope surface water pressure power $\dot{W}_{\mathrm{p}}$ is given as:

$$\dot{W}_{\mathrm{p}} = \omega\gamma_{\mathrm{w}} r_0^3 \int_{\theta_{\mathrm{t}}}^{\theta_{\mathrm{h}}} \left(\frac{r_{\mathrm{dc}}}{r_0}\sin\theta - \sin\theta_0 - \frac{H-h_{\mathrm{t}}}{H}\frac{H}{r_0} \right) \cdot \left(\frac{r_{\mathrm{dc}}}{r_0} \right)^2 \cot(\theta+\beta) d\theta \tag{13}$$

(4) Rate of Energy Dissipation

The expression for the rate of energy dissipation of the soil mass above the phreatic surface is given as:

$$D_{\mathrm{c}} = \omega c \int_{\theta_0}^{\theta_{\mathrm{h}}} r^2 \mathrm{d}\theta \tag{14}$$

4.3. Factor of Safety

According to the principle of virtual power, when a coastal slope is in a limit failure state, the external power equals the rate of energy dissipation, which yields:

$$\dot{W}_{\gamma} + \dot{W}_{\gamma'} + \dot{W}_{\mathrm{w}} + \dot{W}_{\mathrm{p}} = D_{\mathrm{c}} \tag{15}$$

Under general conditions, the Strength Reduction Method (SRM) proposed by Bishop [28,29] is widely adopted internationally to evaluate the factor of safety. This approach has become a well-recognized standard in engineering practice, as expressed by the following equation:

$$F_{\mathrm{s}} = \frac{c}{c_{\mathrm{m}}} = \frac{\tan\varphi}{\tan\varphi_{\mathrm{m}}} \tag{16}$$

In the formula, c stands for the cohesion of the soil mass, and φ refers to the internal friction angle. Meanwhile, c_{m} and φ_{m} represent the equivalent shear strength parameters after reduction, namely the reduced cohesion and reduced internal friction angle. Substituting Equation (16) into Equation (15) yields an implicit function equation with multiple variables, expressed as:

$$F_{\mathrm{s}} = (F_{\mathrm{s}}, \theta_0, \theta_{\mathrm{h}}, c_{\mathrm{m}}, \varphi_{\mathrm{m}} \ldots) \tag{17}$$

This implicit function equation has infinite solutions. Among them, the constraint conditions of $0 < \theta_0 < \theta_{\mathrm{h}} < \pi$ must be satisfied, the optimal upper bound value of the factor of safety needs to be searched, and iterations must be performed during the reduction in strength indices. Therefore, this paper adopts the dichotomy method and develops a MATLAB (v2023, The MathWorks Inc., Natick, MA, USA) program for the solution.

5. Analysis of Theoretical Calculation Results

Comparative Verification

The time settings for the numerical simulation are aligned with the two-dimensional theoretical analysis presented in this study. By performing numerical simulations under tidal cyclic loading, the safety factor of the coastal slope is derived. Four distinct scenarios are examined individually: mean sea level, tidal range, soil cohesion, and internal friction angle. The analysis confirms that the evolution trends observed in the theoretical calculation and numerical simulation results are largely consistent. As depicted in Figure 16, the safety factor F_{s} of the coastal slope exhibits a U-shaped cyclic trend, typified by an initial drop followed by a subsequent rebound. Specifically, the safety factor reaches its peak at the conclusion of the flood tide (t = 0 h) and hits its lowest point at the end of the ebb tide (t = 6 h). This result indicates that the slope stability is strengthened during the flood tide, with the highest stability achieved at the end of the flood tide. Conversely, the slope stability weakens during the ebb tide, making the slope most prone to failure at the end of the ebb tide.

As shown in Table 1, the relative error between the simulated and theoretically calculated results shows an overall increasing and then decreasing trend from t = 0 h to t = 12 h, showing convergence; at the initial stage of flood tide, the water level in the slope changes gently and the seepage field is relatively stable, resulting in a high degree of agreement between the theoretical solutions and numerical solutions; however, with the continuous progress of ebb tide, the fluctuation of the phreatic line inside the slope intensifies and the seepage hysteresis effect becomes more prominent, and the simplified assumptions of the theoretical model cannot fully match the complex unsaturated seepage and stress states during the ebb tide period, leading to the error reaching the maximum at t = 6 h (the end of ebb tide). Nevertheless, the difference between the theoretical and numerical solutions under each working condition is small, with the relative errors being small; only

the working conditions with a large tidal range and low shear strength show a slight increase in errors. Overall, through comparative analysis of theoretical and numerical results, this paper concludes that the theoretical calculations are relatively conservative and show good agreement with the numerical results under the studied conditions. Subsequent experimental research and field monitoring can be carried out to further improve and verify the effectiveness and reliability of the established semi-diurnal tidal slope stability calculation model, water level analytical solution and safety factor calculation method proposed in this paper.

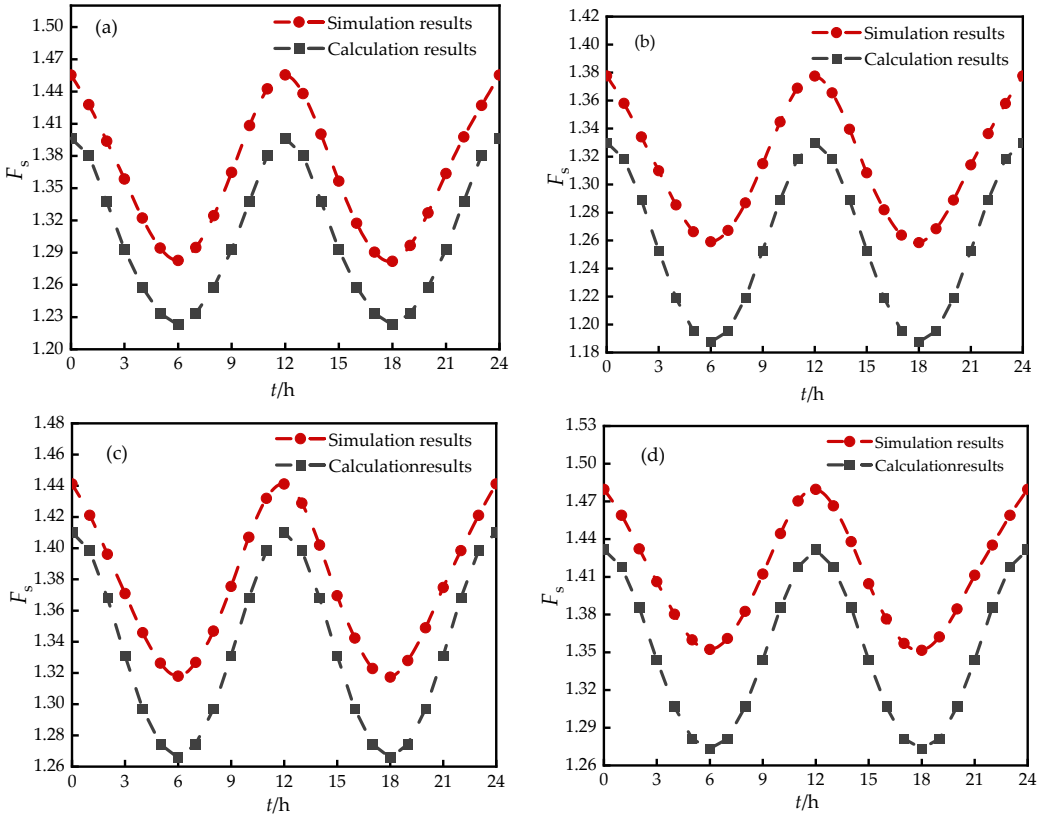


Figure 16. Comparison between calculated results in this paper and simulated results: (**a**) Mean sea level (A = 1 m); (**b**) tidal range (h_0/H = 0.6); (**c**) cohesion (φ = 25°); (**d**) internal friction angle (c = 20 kPa).

Table 1. Comparison of factor of safety between simulated and calculated results at three key time points.

t/h	h_0/H = 0.5			h_0/H = 0.6		
	Simulation	**Theory**	**Error**	**Simulation**	**Theory**	**Error**
0	1.413	1.361	3.81%	1.455	1.397	4.22%
3	1.332	1.273	4.64%	1.359	1.293	5.07%
6	1.265	1.199	5.49%	1.283	1.223	4.91%
9	1.337	1.273	5.04%	1.365	1.293	5.55%
12	1.413	1.361	3.81%	1.455	1.397	4.22%
	A = 1.5 m			A = 2 m		
0	1.416	1.349	5.01%	1.458	1.357	7.39%
3	1.309	1.228	6.62%	1.307	1.193	9.53%
6	1.238	1.136	9.03%	1.219	1.074	13.51%
9	1.316	1.228	7.22%	1.317	1.193	10.34%
12	1.416	1.349	5.03%	1.458	1.357	7.51%

Table 1. *Cont.*

t/h	h_0/H = 0.5			h_0/H = 0.6		
	Simulation	**Theory**	**Error**	**Simulation**	**Theory**	**Error**
	c = 25 kPa			c = 30 kPa		
0	1.441	1.410	2.20%	1.543	1.514	1.92%
3	1.371	1.331	2.99%	1.469	1.432	2.63%
6	1.318	1.266	4.14%	1.411	1.363	3.51%
9	1.375	1.331	3.33%	1.473	1.432	2.90%
12	1.441	1.410	2.20%	1.543	1.514	1.92%
	φ = 28°			φ = 30°		
0	1.480	1.432	3.36%	1.574	1.501	4.88%
3	1.406	1.344	4.64%	1.496	1.406	6.41%
6	1.352	1.273	6.20%	1.439	1.332	8.01%
9	1.412	1.344	5.10%	1.503	1.406	6.85%
12	1.480	1.432	3.35%	1.574	1.501	4.88%

6. Conclusions

(1) The periodic rise and fall of semi-diurnal tide water level causes the phreatic line of coastal slopes to change periodically in synchronization, accompanied by an obvious seepage hysteresis effect. The phreatic line inside the slope reaches its upper limit at the end of flood tide (t = 0 h) and drops to its lower limit at the end of ebb tide (t = 6 h). Pore water pressure changes are concentrated in the slope surface area, while the deep part of the slope is less affected.

(2) Mean sea level height, tidal range, soil cohesion and internal friction angle all exert influences on slope stability. A higher mean sea level correlates with improved overall slope stability, but also leads to a larger fluctuation amplitude of the safety factor. A greater tidal range results in more pronounced stability degradation during the ebb tide phase; meanwhile, a larger drop in water level fluctuation gives rise to a steeper seepage gradient within the slope, elevating the instability risk at the end of ebb tide (t = 6 h). Raising the internal friction angle can boost stability, and increasing cohesion can strengthen stability while mitigating the tidal fluctuation impact.

(3) The stability of coastal slopes exhibits a strong correlation with tidal water level fluctuations. The slope safety factor reaches its minimum at the end of the ebb tide (t = 6 h), corresponding to the most critical condition for slope failure; conversely, it peaks at the end of the flood tide (t = 0 h). Tidal action induces periodic variations in the safety factor primarily by altering the pore-water pressure and stress state within the slope, thus controlling its magnitude and fluctuation amplitude, while having little impact on the position of the slip surface. Under tidal effects, the slope toe and deep slope regions are more prone to reaching the critical instability state with progressive risk accumulation, fully reflecting the concealment and abruptness of tidal impacts on slope stability.

(4) This study investigates the stability evolution of coastal slopes within a semi-diurnal tidal cycle and characterizes the transient responses of the seepage field and safety factor under tidal fluctuations. However, the instability of coastal slopes is usually a long-term process, and repeated saturated–unsaturated alternation and cyclic seepage induced by tidal effects result in cumulative fatigue degradation. Therefore, refined three-dimensional numerical analysis of coastal slope stability can be carried out in future research for long-term prediction, and the combined effect of waves and tides can be considered to better reflect the weakening effect of long-term erosion on soil structure under practical engineering conditions.

Author Contributions: Conceptualization, Y.W. (Yunjun Wei) and J.Z.; Methodology, Y.W. (Yunjun Wei); Software, Y.W. (Yunjun Wei); Validation, Y.W. (Yulong Wang) and J.Z.; Formal analysis, J.Z.; Investigation, C.Y.; Data curation, Y.W. (Yulong Wang); Writing—original draft, Y.W. (Yunjun Wei) and Y.W. (Yulong Wang); Writing—review and editing, Y.W. (Yulong Wang) and C.Y.; Funding acquisition, J.Z. All authors have read and agreed to the published version of the manuscript.

Funding: This work was supported by the National Natural Science Foundation of China (52004088) and the Scientific Research Program of the Higher Education Institutions of Hainan Province, China (Hnky2026ZD-29). The financial support is greatly appreciated.

Data Availability Statement: The raw numerical simulation data (including GeoStudio model files, seepage calculation results, and slope stability safety factor datasets) supporting the conclusions of this article will be made available by the corresponding author on reasonable request. The data are not publicly available due to the large volume of simulation files and the proprietary nature of the model input parameters.

Conflicts of Interest: The authors declare no conflicts of interest.

References

1. Chen, M.; Lv, P.; Zhang, S.; Chen, X.; Zhou, J. Time evolution and spatial accumulation of progressive failure for Xinhua slope in the Dagangshan reservoir, Southwest China. *Landslides* **2018**, *15*, 565–580. [CrossRef]
2. Zhou, J.; Qin, C. Stability analysis of unsaturated soil slopes under reservoir drawdown and rainfall conditions: Steady and transient state analysis. *Comput. Geotech.* **2022**, *142*, 104541. [CrossRef]
3. Gao, Y.; Zhu, D.; Zhang, F.; Lei, G.; Qin, H. Stability analysis of three-dimensional slopes under water drawdown conditions. *Can. Geotech. J.* **2014**, *51*, 1355–1364. [CrossRef]
4. Zeng, L.; Shi, Z.; Fu, H.; Bian, H. Influence of rainfall infiltration on distribution characteristics of slope transient saturated zone. *China J. Highw. Transp.* **2017**, *30*, 25–34.
5. Sun, L.; Tang, X.; Abdelaziz, A.; Liu, Q.; Grasselli, G. Stability analysis of reservoir slopes under fluctuating water levels using the combined finite-discrete element method. *Acta Geotech.* **2023**, *18*, 5403–5426. [CrossRef]
6. Jia, G.W.; Zhan, T.L.; Chen, Y.M.; Fredlund, D.G. Performance of a large-scale slope model subjected to rising and lowering water levels. *Eng. Geol.* **2009**, *106*, 92–103. [CrossRef]
7. Zheng, Y.; Zhao, S. Application of strength reduction fem in soil and rock slope. *Chin. J. Rock Mech. Eng.* **2004**, *23*, 3381–3388.
8. Tian, D.; Zheng, H.; Liu, D. 2D FEM numerical simulation of rainfall infiltration for landslide with considering runoff effect and its application. *Rock Soil Mech.* **2016**, *37*, 1179–1186. [CrossRef]
9. Zhou, Y.; Qi, S.; Fan, G.; Chen, M.; Zhou, J. Topographic effects on three-dimensional slope stability for fluctuating water conditions using numerical analysis. *Water* **2020**, *12*, 615. [CrossRef]
10. Xu, W.; Wang, Y.; Dong, X. Influence of reservoir water level variations on slope stability and evaluation of landslide tsunami. *Bull. Eng. Geol. Environ.* **2021**, *80*, 4891–4907. [CrossRef]
11. Wang, L.; Sun, D.; Li, L. 3D stability of partially saturated soil slopes after rapid drawdown by a new layer-wise summation method. *Landslides* **2019**, *16*, 295–313. [CrossRef]
12. Wei, S.; Ji, F.; Lv, F.; Wang, L. Physical model test on the influence of reservoir water level fluctuation on the deformation of landslides with weak interlayers. *Bull. Eng. Geol. Environ.* **2025**, *84*, 187. [CrossRef]
13. Cao, Z.; Xie, M.; Rong, T.; Du, F.; Li, Z.; Wang, W. Nonlinear seepage mechanical model and bifurcation analysis for fluid-solid coupling in fractured rock mass. *Sci. Rep.* **2026**, *16*, 9578. [CrossRef] [PubMed]
14. Shaikh, B.; Eldho, T. Analytical solution for tide-influenced groundwater variation along sloping complex coastal aquifer in presence of rainfall infiltration. *J. Hydrol. Eng.* **2021**, *26*, 04021036. [CrossRef]
15. Kishore, M.; Santhoshkumar, G.; Parol, V. Pseudodynamic analysis of a bilinear waterfront retaining wall under earthquakes and tsunamis. *Int. J. Geomech.* **2025**, *25*, 04025044. [CrossRef]
16. Kishore, M.; Santhoshkumar, G.; Parol, V. Effects of earthquake and tsunami on the stability of quay walls with a bilinear back face: An analytical study. *Indian Geotech. J.* **2025**, *56*, 525–536. [CrossRef]
17. Sun, Y.; Li, Z.; Yang, K.; Wang, G.; Hu, R. Analysis of the influence of water level change on the seepage field and stability of a slope based on a numerical simulation method. *Water* **2023**, *15*, 216. [CrossRef]
18. Tang, X.; Zheng, Y.; Lin, C. Influence of approach on locating phreatic surface hydrous slope stability analysis. *Chin. J. Rock. Mech. Eng.* **2008**, *27*, 2814–2819.
19. Huang, Y.; Li, M.; Wu, S.; Yang, C. Numerical simulation on slope stability based on continuous-discrete coupling method. *J. Cent. South Univ. (Sci. Technol.)* **2025**, *56*, 1502–1513. [CrossRef]

20. Boruah, P.; Taipodia, J.; Chakraborty, A.; Anshu, A. A systematic review on slope stability and deformation analysis subjected to rainfall and earthquake. *Geotech. Eng. J. SEAGS AGSSEA* **2024**, *55*, 38–52.
21. Li, Z.; Ren, H.; Wang, W.; Du, F.; Huang, Y.; Cao, Z.; Wang, L. Multi-Factor Coupled Numerical Simulation and Sensitivity Analysis of Hysteresis Water Inundation Induced by the Activation of Small Faults in the Bottom Plate Under the Influence of Mining. *Appl. Sci.* **2026**, *16*, 1051. [CrossRef]
22. Wu, Z.; Yang, G.; Li, W.; Chen, X.; Liu, F.; Zheng, Y. Numerical simulation study of rainfall-induced saturated–unsaturated landslide instability and failure. *Water* **2025**, *17*, 2229. [CrossRef]
23. Wang, Y.; Chai, J.; Cao, J.; Qin, Y.; Xu, Z.; Zhang, X. Effects of seepage on a three-layered slope and its stability analysis under rainfall conditions. *Nat. Hazards* **2020**, *102*, 1269–1278. [CrossRef]
24. Chen, S.; Shi, A.; Xu, W.; Yan, L.; Wang, H.; Tian, L.; Xie, W. Numerical investigation of landslide-induced waves: A case study of Wangjiashan landslide in Baihetan Reservoir, China. *Bull. Eng. Geol. Environ.* **2023**, *82*, 110. [CrossRef]
25. Kong, J.; Song, Z.; Xin, P.; Shen, C. A new analytical solution for tide-induced groundwater fluctuations in an unconfined aquifer with a sloping beach. *China Ocean. Eng.* **2011**, *25*, 479–494. [CrossRef]
26. Teo, H.; Jeng, D.; Seymour, B.; Barry, D.; Li, L. A new analytical solution for water table fluctuations in coastal aquifers with sloping beaches. *Adv. Water Resour.* **2003**, *26*, 1239–1247. [CrossRef]
27. Nielsen, P. Tidal dynamics of the water table in beaches. *Water Resour. Res.* **1990**, *26*, 2127–2134. [CrossRef]
28. Liu, S.; Wang, L.; Zhang, W.; Sun, W.; Fu, J.; Xiao, T.; Dai, Z. A physics-informed data-driven model for landslide susceptibility assessment in the Three Gorges Reservoir area. *Geosci. Front.* **2023**, *14*, 101621. [CrossRef]
29. Wei, Y.-J. Study on the Stability of Three-Dimensional Coastal Slopes Under the Influence of Semi-Diurnal Tidal Currents and Rainfall, and Optimization of Anchor Bolt Support. Master's Thesis, Hunan University of Science and Technology, Xiangtan, China, 2026.

Disclaimer/Publisher's Note: The statements, opinions and data contained in all publications are solely those of the individual author(s) and contributor(s) and not of MDPI and/or the editor(s). MDPI and/or the editor(s) disclaim responsibility for any injury to people or property resulting from any ideas, methods, instructions or products referred to in the content.